Materials Horizons

ROYAL SOCIETY OF CHEMISTRY

REVIEW

View Article Online
View Journal | View Issue

Cite this: *Mater. Horiz.*, 2021, **8**, 1367

Recent advances toward environment-friendly photodetectors based on lead-free metal halide perovskites and perovskite derivatives

Ying Li,[a] Zhifeng Shi, *[a] Wenqing Liang,[a] Jingli Ma,[a] Xu Chen,[a] Di Wu, [a] Yongtao Tian,[a] Xinjian Li,*[a] Chongxin Shan[a] and Xiaosheng Fang *[b]

Recently, metal-halide perovskites have emerged as promising materials for photodetector (PD) applications owing to their superior optoelectronic properties, such as ambipolar charge transport characteristics, high carrier mobility, and so on. In the past few years, rapid progress in lead-based perovskite PDs has been witnessed. However, the critical environmental instability and lead-toxicity seriously hinder their further applications and commercialization. Therefore, searching for environmentally stable and lead-free halide perovskites (LFHPs) to address the above hurdles is certainly a worthwhile subject. In this review, we present a comprehensive overview of currently explored LFHPs with an emphasis on their crystal structures, optoelectronic properties, synthesis and modification methods, as well as the PD applications. LFHPs are classified into four categories according to the replacement strategies of Pb^{2+}, including $AB(II)X_3$, $A_3B(III)_2X_9$, $A_2B(I)B(III)'X_6$, and newly-emerging perovskite derivatives. Then, we give a demonstration of the preliminary achievements and limitations in environment-friendly PDs based on such LFHPs and perovskite derivatives, and also discuss their applications in biological synapses, imaging, and X-ray detection. With the perspective of their properties and current challenges, we provide an outlook for future directions in this rapidly evolving field to achieve high-quality LFHPs and perovskite derivatives for a broader range of fundamental research and practical applications.

Received 2nd October 2020,
Accepted 24th December 2020

DOI: 10.1039/d0mh01567a

rsc.li/materials-horizons

1. Introduction

Since Miyasaka and co-workers incorporated $CH_3NH_3PbX_3$ (X = Cl, Br, or I) as a sensitizer into dye-sensitized solar cells and achieved a power conversion efficiency (PCE) of 3.8% in 2009,[1] metal-halide perovskite ABX_3 (A = CH_3NH_3 (MA), NH_2CHNH_2 (FA),

[a] *Key Laboratory of Materials Physics of Ministry of Education, School of Physics and Microelectronics, Zhengzhou University, Daxue Road 75, Zhengzhou 450052, China. E-mail: shizf@zzu.edu.cn, lixj@zzu.edu.cn*

[b] *Department of Materials Science, Fudan University, Shanghai 200433, China. E-mail: xshfang@fudan.edu.cn*

Ying Li

Ying Li received her bachelor degree in physics from Zhengzhou University in 2016. Currently, she is pursuing her PhD at School of Physics and Microelectronics, Zhengzhou University. Her current research focuses on all-inorganic halide perovskite materials and their applications in photodetectors.

Zhifeng Shi

Zhifeng Shi is currently an Associate Professor of School of Physics and Microelectronics, Zhengzhou University. He received his PhD degree in microelectronics and solid-state electronics under the supervision of Prof. Guotong Du at Jilin University. His research interests relate to the controllable synthesis and photophysics of semiconductor optoelectronic materials and their applications in functional devices.

or Cs; B = Pb; X = Cl, Br, I, or mixed halides) solar cells have been widely studied and their PCE has exhibited a rapid rise within the past decade.[2,3] The current certified PCE of perovskite solar cells has surpassed 25.5%,[4] which could be compared to that of single crystal silicon-based solar cells. The reason for such remarkable photovoltaic behaviors of metal-halide perovskites can be attributed to their superior optoelectronic properties, including direct bandgap, large light absorption coefficient, suitable and adjustable bandgap, long carrier diffusion length, and high defect tolerance.[5–7] Moreover, with the increase of the understanding on fundamental material characteristics and device operation principles, the rapid development also extends the applications of perovskite materials beyond photovoltaics to other fields, such as light-emitting diodes (LEDs),[8–10] photodetectors (PDs),[11–16] lasers,[17–21] image sensors,[22–26] memory,[27–30] and so on. These research areas offer a vast platform for perovskite materials, facilitating their applications in the cost-effective and large-scale manufacture of optoelectronics and suggesting new potential.

As a significant constituent of electronic circuits and optoelectronic devices, PDs are capable of transforming light signals (electromagnetic radiation carrying energy) into electric signals based on various principles, which are attracting increasing interest in both academic and industrial domains in a wide range of applications, including light communication, security surveillance, environmental monitoring, image sensing, and space exploration. By employing perovskite materials as the light absorbers, many breakthroughs in developing high-performance and low-cost perovskite PDs have been witnessed in recent years.[31–35] At present, perovskite-based PDs with different geometries and working modes have been successfully demonstrated, such as photoconductors, photodiodes, and phototransistors, and the optimal photoresponsivity exceeds 10^9 A W^{-1}, the specific detectivity (D^*) is up to 10^{16} jones (1 jones = 1 cm $Hz^{1/2}$ W^{-1}), and the response speed reaches the nanosecond level.[12–16] It is worth noting that the obtained photodetection performances of perovskite-based PDs have already attained a level of competitiveness over those based on conventional photo-sensing materials and commercial silicon. Despite the great advances and extraordinary potential, the toxicity issue and intrinsic material instability against moisture, heat, and light irradiation of the commonly used lead-halide perovskites hinder their practical applications and future commercialization.[36–38] To remedy the lead toxicity issue, researchers have made increasing efforts to screen appropriate perovskite alternatives both in theory and experiment. In order to retain the advantages of Pb-based perovskite materials, the electronic configuration of the typical lead-halide perovskites should be considered where the valence band is made up of p-orbitals of halide and s-orbitals of Pb, while the conduction band is only based on lead's p-orbitals.[39,40] Thus, the elements following the order of Pb electronic configuration are preferred as potential alternatives. Therefore, some homovalent (such as Sn and Ge) or heterovalent elements (such as Bi, Sb, Cu, In, and Ag) have been employed as the replacements of Pb.[41–47] By now, Sn(II), Sn(IV), Ge(II), Bi(III), Sb(III), In(III), Ag(I), Cu(I), and Cu(II) have been employed as the replacements of Pb, and some of the produced lead-free halide perovskites (LFHPs) or perovskite derivatives show remarkable optoelectronic properties, which are comparable to the lead-based perovskites or even better in some aspects. Moreover, these encouraging lead-free candidates have low toxicity and high stability. To the best of our

Xinjian Li

Xinjian Li is a Professor of School of Physics and Microelectronics, Zhengzhou University. He received his PhD degree from University of Science and Technology of China. His research interests relate to luminescent materials, energy conversion materials and photoelectric devices.

Chongxin Shan

Chongxin Shan is a Professor of Zhengzhou University. He received his BS degree from Wuhan University in 1999, and PhD degree from Changchun Institute of Optics, Fine Mechanics and Physics, Chinese Academy of Sciences in 2004. His current research focuses on semiconductor optoelectronic materials and devices. He has been supported by National Science Fund for Distinguished Young Scholars, Distinguished Professor of Changjiang Scholars, etc.

Xiaosheng Fang

Xiaosheng Fang received his PhD degree from the Institute of Solid State Physics, the Chinese Academy of Sciences, in 2006. Afterward, he worked at the National Institute for Materials Science (NIMS), Japan as a JSPS postdoctoral fellow and ICYS-MANA researcher. Currently, he is a Professor in the Department of Materials Science, Fudan University, China. His research focuses on inorganic semiconductor-based photodetectors.

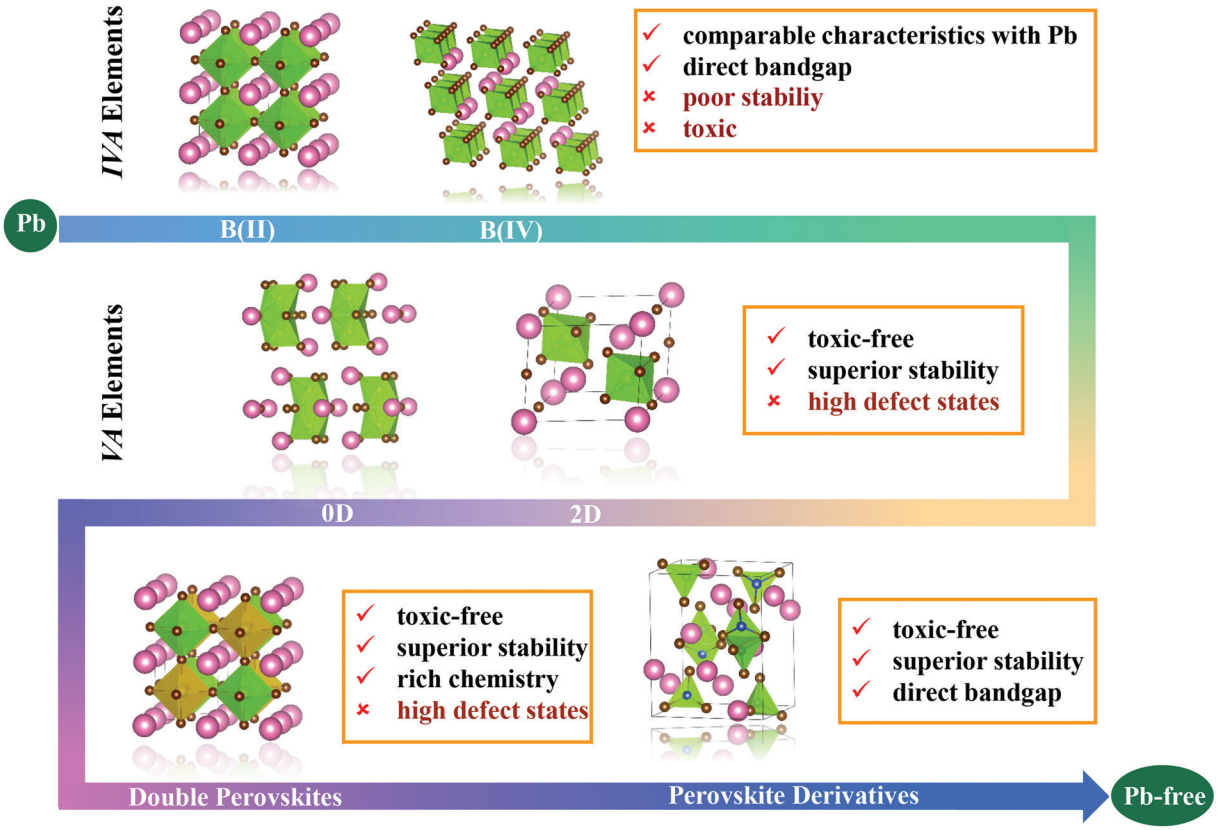

Scheme 1 Schematic illustrations of the approaches and consequences of potential lead replacements.

knowledge, several reviews and perspectives about LFHP synthesis, particularly focused on their photovoltaic applications, have been published.[48–50] However, no study has yet presented a comprehensive overview on LFHP-based photodetection applications.

In this review, we deliver a comprehensive overview on LFHPs and their applications in PDs. Firstly, we give a summary of the approaches and consequences of lead replacements reported in the literature, as shown in Scheme 1. Based on the different replacement strategies, the LFHPs were classified into four categories, including $AB(II)X_3$, $A_3B(III)_2X_9$, $A_2B(I)B(III)'X_6$, and the newly emerging perovskite derivatives. The crystal structure, synthesis method, optoelectronic properties, and environmental stability of each type of material were also analyzed and compared. Then, we give a demonstration of the recent advances in widely studied LFHPs and perovskite derivatives as light absorbers in PDs. Finally, we present current and existing limitations and future development opportunities in this important field.

2. Crystal structure and optoelectronic properties of LFHPs and perovskite derivatives

Typically, the $APbX_3$ structure of perovskite is cubic, and it assembles into a three-dimensional (3D) network by sharing the $[PbX_6]^{4-}$ octahedral corners, where Pb(II) cations are located at the center of the octahedra and the cavity among adjacent octahedra is occupied by A(I) cations. The study of LFHPs was firstly performed by homovalent substitution of Pb(II) with group IVA elements, Sn(II) and Ge(II), in the perovskite structures because of their same valence and comparable ionic radius. Subsequently, various types of LFHPs based on Bi(III), Sb(III), In(III), Ag(I), Cu(I), and Cu(II) replacements were intensively investigated and developed. Various substitutions offer a wide diversity of crystal structures, optical, electrical and other physicochemical properties for LFHPs or perovskite derivatives. The crystal structures of currently explored LFHPs or perovskite derivatives can be summarized as follows.

2.1. Lead replacements by homovalent Sn/Ge elements

Among commonly studied lead substitutions, only Sn and Ge can form the traditional perovskite structure because they both fulfill the coordination and charge balance pre-condition, thereby avoiding the significant lattice disturbance caused by the substitution.[7] Because of the same lone-pair s orbitals, the Sn/Ge-based perovskites have comparable electronic and band structures, as well as remarkable optoelectronic properties and high defect tolerance to the lead analogues.[38] As shown in Fig. 1a, $ASn(II)X_3$ is composed of a 3D network of corner-sharing $[SnX_6]^{4-}$ octahedra, with A cations occupying the cavity among adjacent octahedra. Umari *et al.* investigated the optoelectronic properties of $MASnI_3$ *via* the spin–orbit coupling-GW (SOC-GW) calculation, as shown in Fig. 1c. The band structure of $MASnI_3$

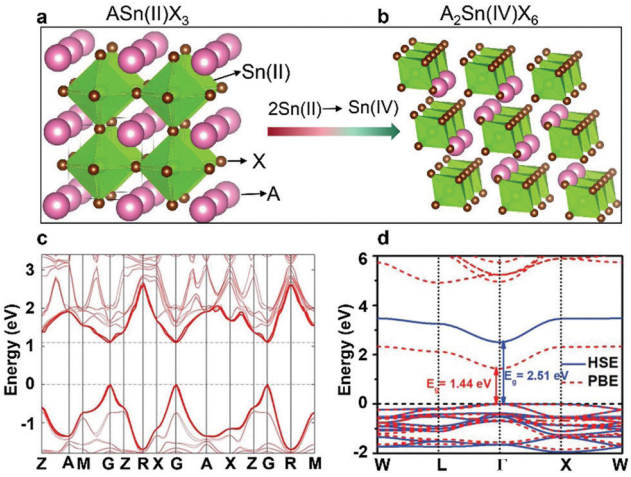

Fig. 1 Crystal structures of (a) $ASn(II)X_3$, and (b) $A_2Sn(IV)X_6$. Calculated band structure of (c) $MASnI_3$ by SOC-GW. Reprinted with permission from ref. 51. Copyright 2014 Nature Publishing Group. Calculated electronic band structures of (d) Cs_2SnBr_6 from the PBE and HSE calculations. Reprinted with permission from ref. 42. Copyright 2019 WILEY-VCH.

exhibits a direct bandgap of 1.1 eV at the Γ point, which is consistent with the experimental bandgap of $\sim$1.3 eV.[51] As a result, the absorption edge of $MASnI_3$ locates at the near-infrared region that is unattainable with lead-based perovskites, which is expected to produce a broader spectral response than Pb-based PDs. Despite this, the applicaitions of $ASn(II)X_3$ perovskites in optoelectronic devices remain highly unsatisfactory at present. On one hand, the Sn^{2+} and Ge^{2+} tend to be oxidized into Sn^{4+} and Ge^{4+} in the air because of the lack of inert pair effect as in Pb^{2+}, resulting in great concern regarding their stability.[37] On the other hand, the high-energy-lying Sn $5s^2$ states make the Sn–I bonds easy to break, forming high-density Sn vacancies. The relatively low formation energy of the Sn vacancy in $ASn(II)X_3$ introduces deep carrier recombination centers, resulting in a substantial device degradation. Therefore, to facilitate their applications in optoelectronic devices, efforts must be made to mitigate the instability issue. It is possible to incorporate additives or donor elements to suppress the oxidation of Sn(II) to Sn(IV). Of course, substitution of Sn(II) with more stable Sn(IV) is another attractive option, though the composition and crystal structure of the Sn(II)-based perovskites need to be modified to maintain the charge balance. As illustrated in Fig. 1b, one Sn(IV) ion and a vacancy replace two Sn(II) ions in $ASn(II)X_3$ perovskites to form vacancy-ordered perovskites, which are composed of a face-centered lattice of SnX_6 units with A cations occupying the cuboctahedral voids. It can be found that the close-packed anionic lattice similar to $ASn(II)X_3$ perovskites is preserved, so the crystal structure is similar to $ASn(II)X_3$.[38] Taking Cs_2SnBr_6 as an example, Fig. 1d shows its band structures calculated by both the Perdew–Burke–Ernzerhof (PBE) and Heyd–Scuseria–Ernzerhof (HSE) approaches. It can seen that the Cs_2SnBr_6 features a direct bandgap, and the calculated HSE/PBE bandgaps are 2.51/1.44 eV, respectively, consistent with the experimental results obtained by Zhou and co-workers.[42]

2.2. Lead replacements by heterovalent Bi/Sb elements

Trivalent B(III) cations, *i.e.*, Bi^{3+} and Sb^{3+}, with similar ns^2 electronic configuration, electronegativity, and a comparable ionic radius with Pb, have attracted significant interest as potential candidates for LFHPs. First, their similar ns^2 electronic configuration with Pb tends to establish an anti-bonding interaction at the valence band maximum (VBM); thus the defects were confined to the shallow states at energy band edges. Therefore, even with defective sites, the optoelectronic properties of B(III) cations may be retained. Second, Bi^{3+} and Sb^{3+} cations possess a large absorption coefficient of $\sim 10^5$ cm^{-1} comparable to Pb-based materials, which is determined by the absorption between X-5p valence states and 6p absorption states.[52] Moreover, the optical transition from 6s states (near the VBM) to 6p conduction states also contributes to the large absorption coefficient.[53] Third, a long carrier diffusion lifetime for Bi/Sb-based perovskites is expected due to their octahedral coordinated structure. These impressive properties make Bi/Sb promising candidates to replace the toxic Pb. For such heterovalent substitutions, the chemical formula is $A_3B(III)_2X_9$, which is equivalent to that obtained by removing 1/3 of the B-site cations from ABX_3.[7,37,50,54,55] The $A_3B_2X_9$ compounds have two typical structures: one is the 0D dimer form composed of isolated face-sharing $[B_2X_9]^{3-}$ octahedra (Fig. 2a), and the other is the 2D layered perovskite (Fig. 2b). The preferential formation of two competing structures depends on the selection of A, B, and X ions. For example, $Cs_3Bi_2I_9$,[54] $MA_3Bi_2I_9$,[56] and $MA_3Sb_2I_9$[57] show isolated face-sharing octahedra, whereas $(NH_4)_3Sb_2I_9$,[58] $MA_3Sb_2Cl_xI_{9-x}$,[59] and $Rb_3Sb_2I_9$,[60] show a 2D layered perovskite structure. For 2D layered perovskite $Cs_3Bi_2I_9$, Liu *et al.* reported their calculated electronic band structure (Fig. 2d), with a bandgap of 2.24 eV.[61] Similar to the lead-based perovskites, the bandgap of $Cs_3Bi_2X_9$ can also be adjusted from 2.11 to 3.15 eV after a simple halogen adjustment, which is advantageous for realizing detection in the visible light range.[62] Moreover, theoretical and experimental studies indicated that Bi-based perovskites demonstrated better material stability than that of conventional lead-halide perovskites. Using first-principles calculations, Ma and co-workers observed that the decomposition energy of trigonal $Cs_3Bi_2Br_9$ is much higher than that of cubic $CsPbBr_3$ (Fig. 2e), which may be due to the shortened bond length and additional distortion of the $[BiBr_6]^{3-}$ octahedron. Furthermore, they extended the theoretical investigation into the migration of native defects (*i.e.*, Br vacancy, V_{Br}^{+}) in perovskites. As seen in Fig. 2f, the diffusion barrier of V_{Br}^{+} in $Cs_3Bi_2Br_9$ is much higher than that in $CsPbBr_3$ indicating the chemical stability of $Cs_3Bi_2Br_9$. Experimentally, the authors also systematically evaluated the effect of ultraviolet (UV) light, heat, and moisture/oxygen on the optical and structural performance of such materials. The result is consistent with the theoretical data discussed above. For $Cs_3Sb_2X_9$ LFHPs, their stability study and related results are similar to those of $Cs_3Bi_2X_9$,[63] and the above theoretical analysis is also applicable.

A fact that should be recognized is that the replacement of Pb by Bi or Sb can reduce the dimensionality of the perovskite

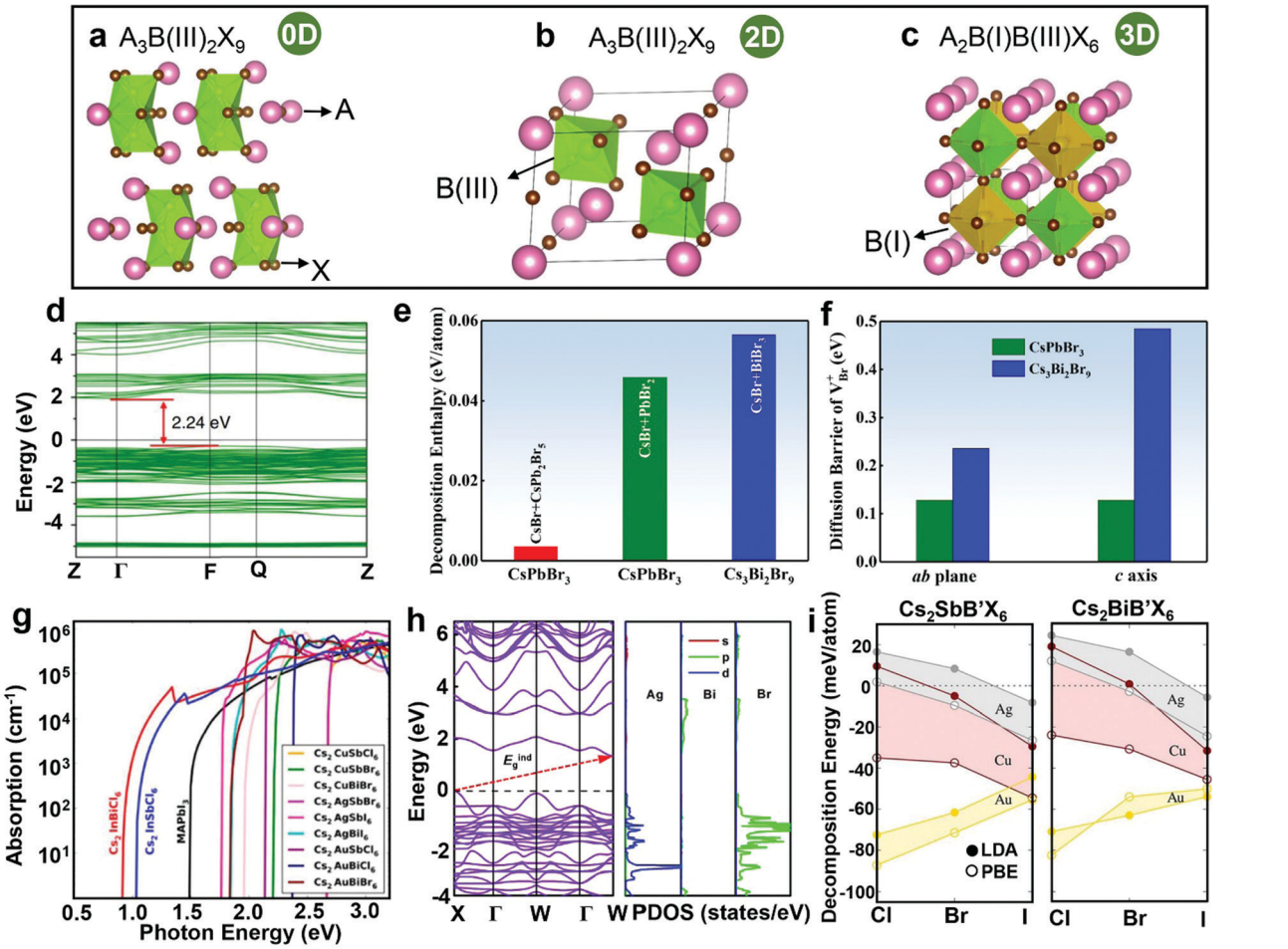

Fig. 2 Crystal structures of (a) 0D $A_3B(III)_2X_9$, (b) 2D $A_3B(III)_2X_9$, and (c) $A_2B(I)B(III)X_6$ LFHPs. (d) Calculated electronic band structure of $Cs_3Bi_2I_9$. Reprinted with permission from ref. 61. Copyright 2020 Nature Publishing Group. Comparison of the (e) decomposition enthalpies, and (f) diffusion barriers of V_{Br}^+ in $Cs_3Bi_2Br_9$ and lead-halide perovskites. Reprinted with permission from ref. 62. Copyright 2020 Royal Society of Chemistry. (g) Calculated absorption spectra of selected optimal $A_2BB'X_6$ perovskites passing the screening process. Reprinted with permission from ref. 64. Copyright 2017 American Chemical Society. (h) Calculated band structure and PDOS spectra of $Cs_2AgBiBr_6$. Reprinted with permission from ref. 65. Copyright 2019 WILEY-VCH. (i) Stability of Sb- and Bi-based halide double perovskites with respect to their decomposition energies using the local density approximation and PBE functions with different approximations. Reprinted with permission from ref. 68. Copyright 2018 American Chemical Society.

structure, leading to reduced band dispersion, increased effective masses of charge carriers, and decreased carrier mobility.[7] To avoid the issues noted above, halide double perovskites with B-site substitution by mixed cations (B = B(I), B′ = B(III)) have been recently explored to form 3D LFHPs ($A_2BB'X_6$), as illustrated in Fig. 2c. The crystal unit of halide double perovskites is very similar to that of lead-based perovskites. The difference is that the B-site cations are alternately arranged by mixed cations (B = B(I), B′ = B(III)) to occupy the octahedral center. The crystal structure shows that it is a face-centered cubic structure with space group *Fm3m* and the 3D structure was maintained. The halide double perovskites offer tremendous options, since a wide range of different elements are available for B(I) and B(III) ions. Through the strategy of cation-transmutation and the density-functional-theory (DFT) method, Zhao *et al.* theoretically explored 64 members of the $A_2BB'X_6$ materials, where A is Cs^+, B represents monovalent cations Na^+, K^+, Rb^+, Cu^+, Ag^+, Au^+, In^+, and Tl^+, B′ is trivalent cations of Bi^{3+}or Sb^{3+}, and X is a halogen (Cl^-, Br^-, and I^-).[64] Considering the excellent phase stability, small carrier effective masses, and low exciton binding energies, eleven of them were predicted as promising materials to replace lead-halide perovskites. Fig. 2g shows the calculated absorption spectra of selected $A_2BB'X_6$ perovskites. Fig. 2h displays the calculated electronic band structure of $Cs_2AgBiBr_6$, one of the most studied materials.[65] The coupling between Ag(d) + Bi(s) and anionic X(p) states makes the VBM decenter at point X in the Brillouin zone, resulting in an indirect bandgap of 2.09 eV.[66,67] In addition, Filip *et al.* calculated the thermodynamic stabilities of $A_2BB'X_6$ (B = Cu, Ag, and Au; B′ = Bi, and Sb; and X = Cl, Br, and I).[68] Fig. 2i shows the stability with their decomposition energies (ΔH), and one can observe that the compounds with decomposition values below zero are unstable. Further investigations showed that solid solutions such as $Cs_2BiAg_{1-x}Cu_xCl_6$ are stable. Overall, the halide double perovskites have rich combinatorial chemistry and significantly enhanced thermodynamic

stability, so they have great potential in a wide range of optoelectronic/electronic applications.

2.3. Perovskite derivatives

In addition to the vast study of the above metals, some other metal cations have also been investigated, such as Cu, and In, forming low-dimensional perovskite derivatives due to their smaller ion radii than that of Pb cations. Recently, such perovskite derivatives, which refer to metal halides without clear relation to the perovskite structure, have become a research hotspot. Also, these halide semiconductors exhibit superior stability and direct bandgap. Here, we take Cu^{+}, Cu^{2+}, and In^{3+} as examples, focusing on their crystal structures and electronic band structures. Fig. 3a shows the crystal structure of $CsCu_2I_3$. Each $[CuI_4]^{-}$ tetrahedron is connected by three common edges to form a 1D chain structure. The Cs^{+} ions are located between every two chains, which are coordinated by eight I^{-} ions in the form of double-capped trigonal prisms. The electronic band structure of $CsCu_2I_3$ was calculated using the PBE functional.[69] As shown in Fig. 3b, $CsCu_2I_3$ is calculated to possess a direct bandgap (2.15 eV), with the VBM and CBM both being at the *G* point. In addition, such copper halides exhibit excellent carrier transport properties due to the highly dispersive bands near the valence and conduction edges.[70] Fig. 3c shows the 0D crystal structure of $Cs_3Cu_2I_5$, in which a tetrahedral site and a trigonal site are formed. Both of them form $[Cu_2I_5]^{3-}$ and each $[Cu_2I_5]^{3-}$ is separated by surrounding Cs^{+} ions. The electronic band structure of

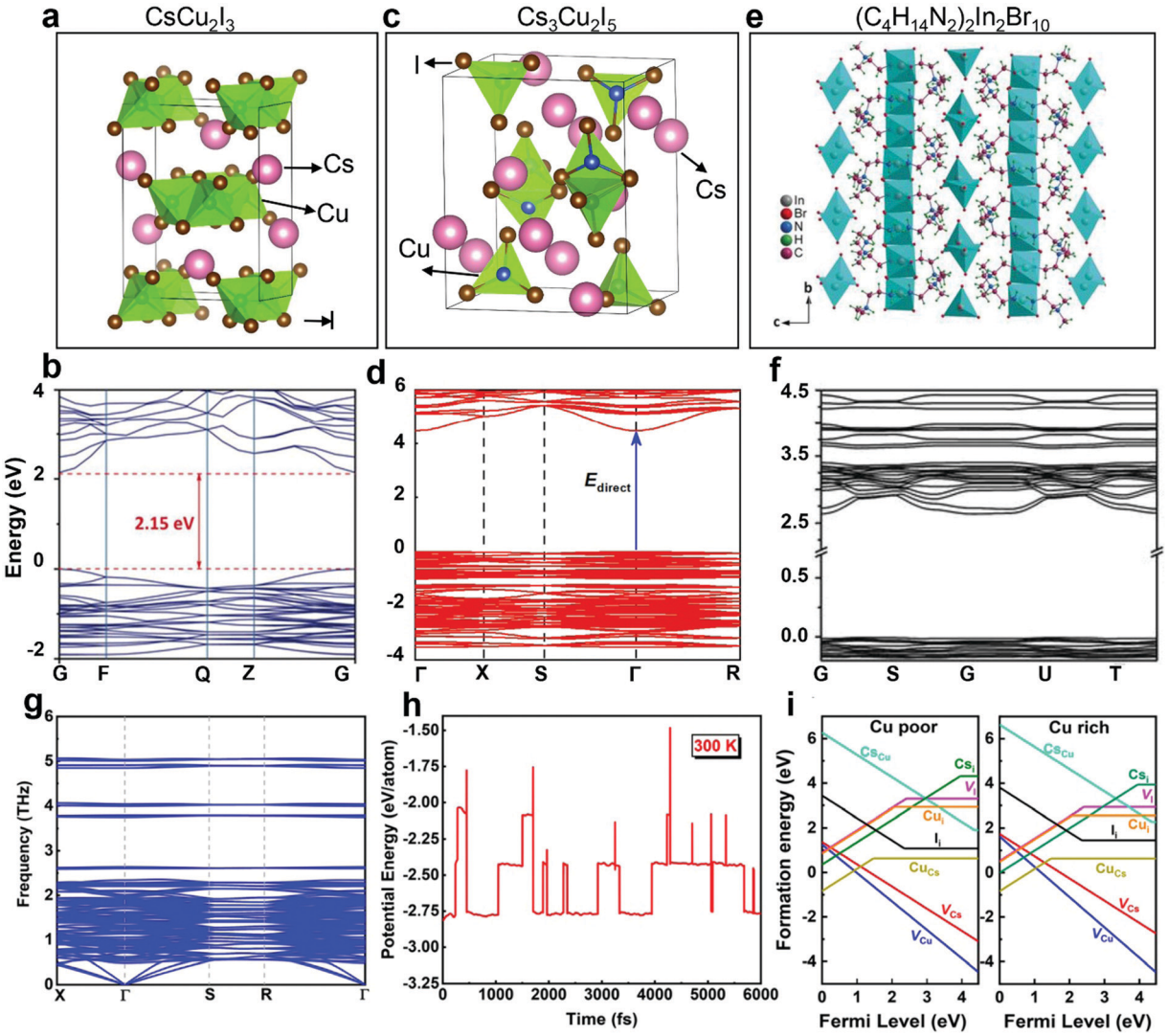

Fig. 3 (a) Crystal structure, and (b) electronic band structure of $CsCu_2I_3$. Note that the bandgap is underestimated by the PBE calculations. Reprinted with permission from ref. 69. Copyright 2020 WILEY-VCH. (c) Crystal structure, and (d) electronic band structure of $Cs_3Cu_2I_5$. Reprinted with permission from ref. 72. Copyright 2020 American Chemical Society. (e) Crystal structure, and (f) electronic band structure of $(C_4H_{14}N_2)_2In_2Br_{10}$. Reprinted with permission from ref. 71. Copyright 2019 WILEY-VCH. (g) Phonon band structure of the $Cs_3Cu_2I_5$. (h) Potential energy fluctuations of $Cs_3Cu_2I_5$ as a function of the molecular dynamic simulation step at 300 K. (i) Formation energies of the intrinsic vacancy defects as a function of Fermi level. Reprinted with permission from ref. 72. Copyright 2020 American Chemical Society.

$Cs_3Cu_2I_5$ was calculated using the PBE functional,[72] and it is characterized by a direct bandgap (Fig. 3d). In addition, the $K_2Cu_2Cl_6$ (Cu^{2+}) material was also synthesized by Zhou and co-workers,[47] which is characterized by a monoclinic structure with the space group of $P_2(1)/C$, and the $[Cu_2Cl_6]^{2-}$ dimers are located at the corners and center of the unit cell in the *b–c* plane. The band structure of $K_2Cu_2Cl_6$ possesses a bandgap of about 0.26 eV along the highly symmetric points. Fig. 3e shows the crystal structure diagram of $(C_4H_{14}N_2)_2In_2Br_{10}$, in which the separated $[InBr_6]^{3-}$ octahedrons and $[InBr_4]^-$ tetrahedrons are surrounded by the cations respectively, forming a characteristic 0D structure at the molecular level.[71] In addition, the hydrogen bond was not found between $[C_4H_{14}N_2]^{2+}$ cations with $[InBr_4]^-$ tetrahedrons, but it was found in $[InBr_6]^{3-}$ octahedrons, suggesting that the tetrahedrons are highly isolated in $(C_4H_{14}N_2)_2In_2Br_{10}$, further confirming its 0D structure. The DFT calculations (Fig. 3f) show that the highest occupied molecular orbitals (HOMOs) for $(C_4H_{14}N_2)_2In_2Br_{10}$ are constituted by completely flat bands, reflecting that the electronic states are highly localized owing to the confined charge carriers. From the stability point of view, all-inorganic perovskite derivatives generally exhibit better stability compared to their lead-based counterparts. Taking $Cs_3Cu_2I_5$ as an example, Wang *et al.* studied the dynamic stability and thermodynamic stability of $Cs_3Cu_2I_5$ through first-principles calculations.[72] First, no negative frequency was observed from the phonon band structure; thus the dynamic stability of $Cs_3Cu_2I_5$ was proved, as shown in Fig. 3g. Then, the calculation of the decomposition enthalpy at 0 K and the first-principles molecular dynamics simulation at 300 K were performed (Fig. 3h), and the results show that $Cs_3Cu_2I_5$ has a good thermodynamic stability. In addition, in order to understand the defect state in $Cs_3Cu_2I_5$, they analyzed the relationship between the formation energy of inherent defects and the Fermi level under Cu-poor and Cu-rich chemical growth conditions (Fig. 3i). It can be seen that under two growth conditions, the formation energy of the Cu vacancy (V_{Cu}) is the lowest. Fortunately, the nondiffusion of V_{Cu} in the $[Cu_2I_5]^{3-}$ cluster may contribute to its robust stability.

3. LFHPs and perovskite derivatives as light absorbing layer for PDs

Due to their exceptional optoelectronic properties and excellent stability, LFHPs and perovskite derivatives have been used extensively for PD applications. In this section, we aim to summarize the recent advances in widely studied LFHP and perovskite derivative PDs and delve into the progress in understanding their synthesis method, optimization strategy, and optoelectronic performance. The main performance parameters of LFHP PDs with different structures and active materials are summarized in Table 1.

3.1. PDs based on Sn-based perovskites

By using the remarkable optoelectronic properties of Sn-based perovskites, much interesting progress has been made. In 2017, Waleed *et al.* fabricated $CH_3NH_3SnI_3$ ($MASnI_3$) nanowire (NW) arrays for the first time in porous alumina templates by using a vapor phase chemical reaction method (Fig. 4a).[73] With this method, the diameter and periodicity of the NWs were precisely controlled, which is highly attractive for photonic and optoelectronic applications. By using the NW arrays as the photoactive material, they fabricated a PD, with photoresponsivity of 0.47 A W^{-1} and D^* of 8.80×10^{10} jones. For this approach, the alumina sidewalls effectively blocked the lateral diffusion path of oxygen and water molecules, so that the material stability was dramatically improved. However, the device performance in their case is still not satisfactory due to the lack of lateral transmission and the long transport distance between the two electrodes. Under these circumstances, Du *et al.* prepared $CsPb_{1-x}Sn_xI_3$ nanobelts (NBs) *via* a solvothermal route, as seen Fig. 4b.[74] Note that the high-quality $CsPb_{1-x}Sn_xI_3$ NBs possess a low density of defects with limited recombination of charge carriers and a high light absorption coefficient. Therefore, the PDs based on a single $CsPb_{0.922}Sn_{0.078}I_3$ NB show a remarkable performance with a photoresponsivity of up to 1.18×10^3 A W^{-1} (Fig. 4c). For PD applications, Sn can be deemed as a suitable Pb substitution mainly for two reasons; the first is the lower toxicity of Sn, and the other is the smaller ionic radius of Sn (Sn^{2+}: 1.35 Å and Pb^{2+}: 1.49 Å), which can broaden the response spectrum of the fabricated PDs.[75–78] For example, Zhu *et al.* demonstrated an efficient low-bandgap Sn-rich binary PD,[76] and the optimized Sn-rich binary PDs can achieve a broad spectral response from 300 to 1100 nm and a high external quantum efficiency (EQE), as shown in Fig. 4d. However, for Sn(II)-based perovskites, the easy oxidation of Sn(II) to Sn(IV) represents a large concern for their stability. Therefore, various methods were conducted to improve the device stability, as shown in Fig. 4e. For example, in 2018, Qian *et al.* reported 2D perovskite $(PEA)_2SnI_4$ flexible film PDs *via* a one-step solution processing method.[79] SnF_2 was added to reduce the Sn vacancies by increasing their formation energy, and inhibit the transition from Sn^{2+} to Sn^{4+}. The structure of the $(PEA)_2SnI_4$ flexible PD is shown in Fig. 4f, in which the flexible electrodes were prepared by patterning the spin-coated rGO (reduced graphene oxide)/(PEDOT:PSS) hybrid films on polyethylene terephthalate (PET) substrates. The conductance of rGO is significantly enhanced due to the introduction of PEDOT:PSS. The obtained device exhibited a photoresponsivity of ~16 A W^{-1}, and D^* of 1.92×10^{11} jones. Moreover, the PD can maintain its initial performance after 1500 cycles of bending, as presented in Fig. 4g. In addition, Liu *et al.* demonstrated a high-performance flexible PD based on the $FASnI_3$ films.[80] By introducing hydroxyl benzene sulfonic acid additive along with excess $SnCl_2$ to form a complex layer to encapsulate the perovskite grains *in situ*, air-stable $FASnI_3$ films were successfully prepared. The device based on the dense $FASnI_3$ layer displays high photoresponsivity in a broad wavelength region from 300 to 1000 nm with the maximum photoresponsivity and gain of over 10^5 A W^{-1} and 10^5, respectively, at a low working voltage. Replacing divalent Pb with Sn(IV) is also an effective method to form a salt structure with the formula of A_2SnX_6 (X = Cl, Br, and I),

Table 1 Summary of the device performance of reported lead-free PDs

Materials (device structure)	Response range (nm)	Responsivity (A W^{-1})	D^* ($\times 10^{12}$ jones)	EQE (%)	t_r/t_d (ms)	Ref.
$Au/CsPb_{0.922}Sn_{0.078}I_3/Au$	300–480	1.18×10^3	64.3	3.63×10^5	240/271	74
$ITO/CsPb_xSn_{1-x}(Br_yI_{1-y})_3/ITO$	400–600	0.0085	0.02	—	4.25/4.82	136
$SnO_2/(FASnI_3)_{0.6}(MAPbI_3)_{0.4}/P3HT$	300–1000	—	0.1	45	35/52	77
$ITO/PTAA/PEAI/ABI/PEAI/C_{60}/BCP/Cu$	300–1050	0.53	0.08	80	—	137
$MoO_3/PEDOT:PSS/CsPb_xSn_{1-x}I_3/PC_{61}BM$	300–1100	0.2	0.1	50	$9 \times 10^{-5}/2.27 \times 10^{-3}$	76
$Cr/Au/(FSA)_2SnI_4$	500–700	—	—	—	0.186/0.3711	41
$PEDOT:PSS/MAPb_{1-x}Sn_xI_3/C60$	300–1000	0.39	7	50	—	78
$Cr/Au/FASnI_3/Cr/Au$	300–1000	10^5	1.9	—	8700/57 000	80
$Au/Cs_2SnCl_{6-x}Br_x/Au$	550–650	—	0.02	—	—	42
$Al/TQB/CsSnBr_3/Au$	400–740	—	—	—	—	138
$rGO/PEDOT:PSS/(PEA)_2SnI_4$	400–650	16	0.192	—	630/3600	79
$Al/MASnI_3/Au$	550–1000	0.47	0.088	—	1500/400	73
$Ti/Au/(FSA)_2SnI_4$	500–1000	0.054	3.85×10^{-7}	—	83.8/243.4	139
$FTO/Cs_2SnI_6/FTO$	500–900	—	—	—	100/100	81
$MWCNT/Cs_2SnCl_6:Bi/GaN$	350–400	0.208	1.2	68.1	$7.5 \times 10^{-4}/9.1 \times 10^{-4}$	82
$FTO/MA_3Bi_2I_9/Ag$	400–700	0.16	4.6	—	26.81/41.98	43
$ITO/Cs_3Bi_2I_9/ITO$	400–600	0.0331	0.02	—	10.2/37.2	88
$Ag/AG_3Bi_2I_9/Ag$	400–700	0.0148	0.088	2.8	0.152/0.187	92
$ITO/Cs_3Bi_2I_9/Au$	350–600	0.0072	0.1	—	0.247/0.23	89
$Au/Cs_3Bi_2I_9/Au$	300–700	1.1	4.7	288	—	61
$ITO/PEDOT:PSS/Cs_3Bi_2I_{9-x}Br_x/C_{60}/BCP/Ag$	300–600	0.015	0.46	—	40.7/27.1	140
$Au/CsBi_3I_{10}/Au$	400–700	21.8	19.3	4130	0.33/0.38	84
$Au/(TMHD)BiBr_5/Au$	200–650	0.152	—	50	8.9/10.2	93
$FTO/(PDM)_2Bi_2I_{10}{\cdot}2H_2O/FTO$	350–600	0.00114	1.9×10^{-6}	0.4	—	87
$ITO/Cs_3BiBr_6/ITO$	300–470	2.5×10^{-5}	8×10^{-4}	0.008	50/60	141
$Au/Cs_3Sb_2Cl_9/Au$	280–500	3616	1.25×10^{-6}	10 959	130/230	44
$ITO/MA_3Sb_2Cl_9/ITO$	400–700	40	1	10 000	0.4/0.9	100
$Au/Cs_3Sb_2Br_9/Au$	300–600	3.8	2.6	—	24/48	99
$Au/Cs_3Sb_2Br_9/Au$	420–500	2.29	3.77	1800	0.2/3	142
$Pt/(MV)[SbI_3Cl_2]/Pt$	250–900	0.03	0.1	6.69	690/280	101
$Au/Cs_2AgInCl_6/Au$	340–400	0.013	1	—	0.97	45
$Au/Cs_2AgBiBr_6/Au$	300–600	7.01	0.566	2146	0.956/0.995	103
$ITO/SnO_2/Cs_2AgBiBr_6/Au$	300–550	0.13	0.024	38.5	3	104
$In/GaN/Cs_2AgBiBr_6/Ag$	200–550	1.46	9.4	—	3.463/8.442	65
$SnO_2/Cs_2AgBiBr_6/TFB/Au$	300–550	0.14	3.29	35	1.7×10^{-5}	107
$ITO/Cs_2AgBiBr_6/ITO$	300–550	5×10^{-5}	0.02	0.01	—	109
$FTO/ALD\text{-}NiO_x/Cs_2AgBiBr_6/TiO_2$	300–550	—	12	—	1.61/1.74	111
$FTO/SnO_2/Cs_2AgBiCl_6/TFB/Au$	300–450	0.01	1	—	—	112
$Ag/Cs_2AgBiBr_6/Ag$	200–600	9×10^{-4}	0.001	—	159/85	113
$Al/Cs_4CuSb_2Cl_{12}/Al$	—	10^{-3}	10^{-4}	—	120/180	46
$FTO/TiO_2/K_2Cu_2Cl_6$	330–390	—	—	—	—	47
$ITO/Cs_3Cu_2I_5/ITO$	200–400	0.0649	1.1×10^{-3}	0.3	26.2/49.9	126
$Au/Cs_3Cu_2I_5/Au$	200–320	17.8	1.12	8321	0.465/0.897	123
$Au/Cs_3Cu_2I_5/GaN/In$	300–370	0.28	1.4	—	0.095/0.13	121
$Au/CsCu_2I_3/Au$	280–350	32.3	1.89	—	0.007/0.214	131
$Ag/CsCu_2I_3/Ag$	300–700	0.052	0.093	7.4	0.19/14.7	132

ABI: $Cs_{0.05}MA_{0.45}FA_{0.5}Pb_{0.5}Sn_{0.5}I_3$; MWCNT: multi-walled carbon nanotube; AG: aminoguanidinium; TMHD: *N*,*N*,*N*,*N*-tetramethyl-1,6-hexanediammonium; PD:PDM; MV: *N*,*N*′-dimethyl-4,4′-dipyridylium.

which is a 50% Sn-deficient perovskite derivative with a $[SnX_6]^{2-}$ octahedron.[42,81,82] This substitution can not only result in a long-term stability in air but also maintain the high-symmetry cubic structure with a different halogen X (X = Cl, Br, and I). Han *et al.* reported a facile hydrothermal method to synthesize Cs_2SnX_6 (X = I and Br) with high crystallinity and yield.[81] To assess the potential applications of Cs_2SnI_6 for optoelectronic devices, they designed and fabricated two-terminal PDs with a simple structure of FTO/Cs_2SnI_6/FTO, as schematically illustrated in Fig. 4h. The devices exhibit a fast response speed with rise time (t_r) and decay time (t_d) both less than 100 ms. Except for the photoconductive type PDs, another heterojunction device was also prepared from Bi-doped Cs_2SnCl_6 nanoparticles (NPs) spin-coated on GaN substrate (Fig. 4i).[82] Due to the construction of a type II heterojunction and the good crystallization of the NPs, the device exhibits a fast response speed (t_r/t_d = 0.75/0.91 μs).

3.2. LFHP-based PDs through heterovalent element substitution

3.2.1. Bi-based halide perovskites. In 2017, Wessels *et al.* reported the synthesis of $Cs_3Bi_2I_9$ and $Rb_3Bi_2I_9$ single crystals (SCs), and they pointed out that the large bandgap, high resistivity, and photoresponse are key characteristics for hard radiation PD materials.[83] In the same year, Tong *et al.* synthesized the $CsBi_3I_{10}$ films by a simple solution process,[84] in which chloroform was used to accelerate the evaporation of the solvent, and then dried under vacuum, as shown in Fig. 5a. The treated films show a highly smooth surface and a high

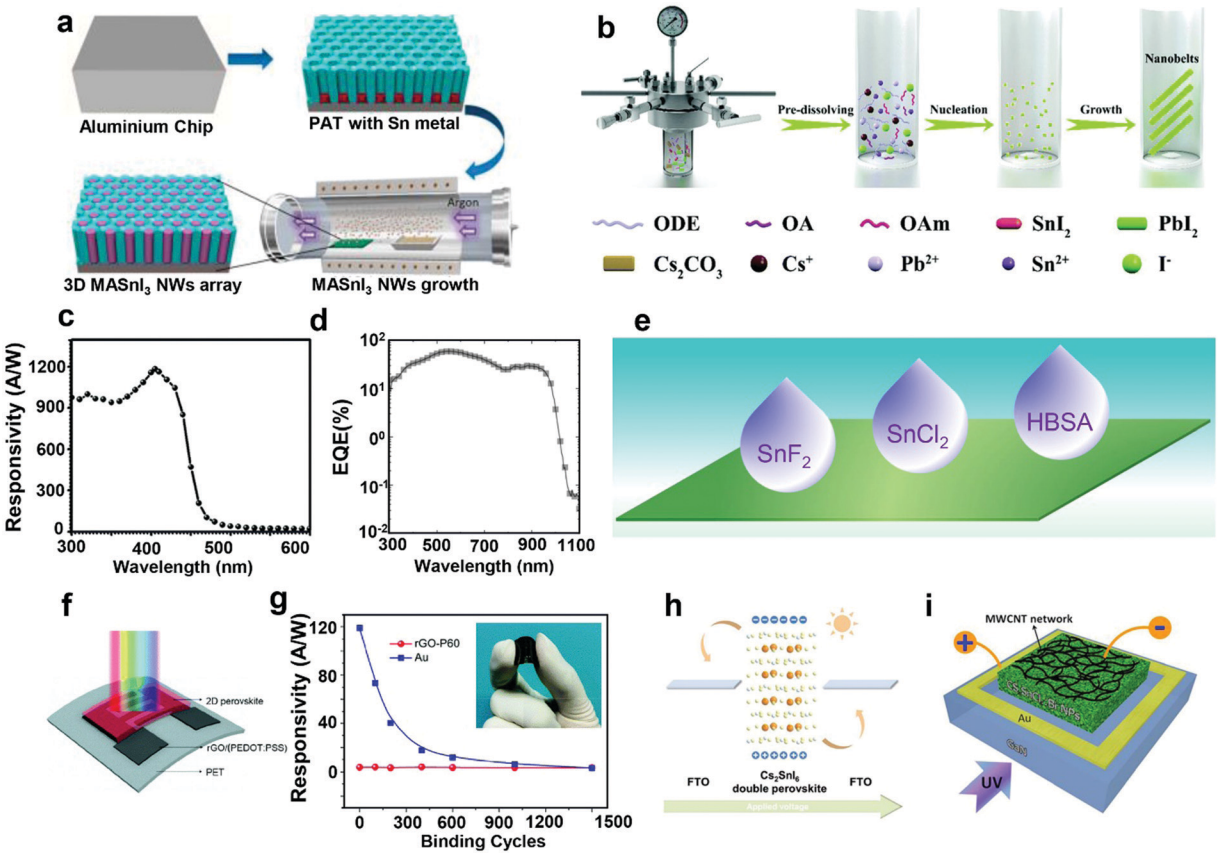

Fig. 4 (a) Growth schematic for Sn-based perovskite NWs by vapor diffusion of MAI. Reprinted with permission from ref. 73. Copyright 2017 American Chemical Society. (b) Schematic diagram of the synthesis process for $CsPb_{1-x}Sn_xI_3$ NBs. (c) Representative spectral response of the PDs with the wavelength ranging from 300 to 600 nm at a bias of 2 V. Reprinted with permission from ref. 74. Copyright 2018 Royal Society of Chemistry. (d) EQE against the wavelength of incident light. Reprinted with permission from ref. 76. Copyright 2019 American Chemical Society. (e) Additive engineering to maintain Sn in its bivalent state. (f) Device structure of a $(PEA)_2SnI_4$ flexible PD. (g) The inset is a picture of the flexible device with rGO/(PEDOT:PSS) electrode. Plots of photoresponsivity against the bending cycle number for the flexible device with the Au electrode or rGO-P60 electrode (5.5 mm radius, and 412 μW cm^{-2} irradiance at 470 nm). Reprinted with permission from ref. 79. Copyright 2018 Royal Society of Chemistry. (h) Schematic working mechanism of FTO/Cs_2SnI_6/FTO. Reprinted with permission from ref. 81. Copyright 2019 WILEY-VCH. (i) 3D schematic illustration of the Cs_2SnCl_6:Bi/GaN heterojunction photodiode. Reprinted with permission from ref. 82. Copyright 2019 American Institute of Physics.

crystalline quality; thus the as-assembled device has a high optoelectronic performance under light illumination (400–700 nm) (Fig. 5b). In addition to the photoconductive PDs, self-powered PDs have also been widely studied.[43,85–87] For example, based on the $MA_3Bi_2I_9$ microcrystalline films, Hussain and co-workers fabricated a self-powered PD with asymmetric contact electrodes (FTO/$MA_3Bi_2I_9$/Ag), as illustrated in Fig. 5c.[43] The PD exhibited a remarkable performance with high photosensitivity of 10^5 and D^* of 10^{12} jones at low operating voltages, as seen in Fig. 5d. It was also revealed that the $MA_3Bi_2I_9$ PD had a good stability after storage for two months at ambient conditions. Recently, Pious *et al.* reported a novel LFHP material, $(1,3\text{-propanediammonium})_2Bi_2I_{10}{\cdot}2H_2O$.[87] As illustrated in Fig. 5e, the $[Bi_2I_{10}]^{4-}$ was formed by the edge sharing of $[BiI_6]^{3-}$ octahedra, and the well-aligned inorganic units and the sandwiched organic cation layers on either side form a quantum-well structure. The optoelectronic applications were demonstrated, indicating the possibility of such a material as a promising candidate for photodetection.

However, there are many obstacles that impede the further improvement of the performance of film-based PDs; for example, there are a large amount of grain boundaries and defects in polycrystalline material forms, by which the photogenerated carriers would be rapidly trapped. Therefore, it is very important to enhance the integrity of the light absorbers. In this regard, Pan and co-workers synthesized highly stable and lead-free $Cs_3Bi_2I_9$ perovskite NPs for photodetection applications through a solution-process method.[88] Fig. 5f shows the typical optical images of the obtained $Cs_3Bi_2I_9$ NPs grown on Au film, sapphire, PDMS, glass, and SiO_2/Si substrates. The corresponding atomic force microscope (AFM) image of the NPs on SiO_2/Si substrate shows a low surface roughness of 1 nm, indicating a good crystal quality. The PDs constructed with these NPs display a maximum photoresponsivity of 33.1 mA W^{-1} under the illumination of a 450 nm laser. Due to the good crystallization and high defect tolerance of $Cs_3Bi_2I_9$ NPs, the device exhibits high stability. Besides, a $Cs_3Bi_2I_9$ SC thin film with a high quality was grown on the ITO glass by a space-limited

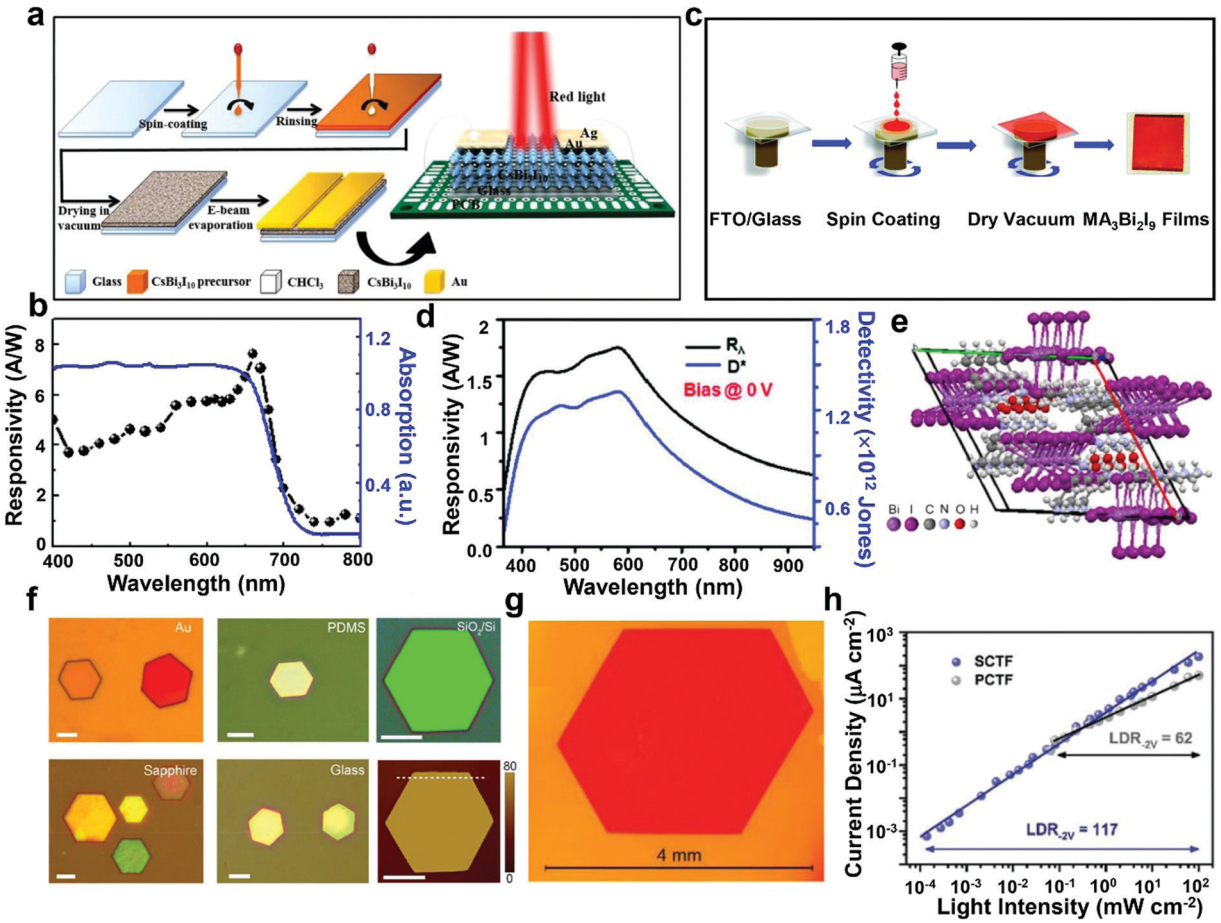

Fig. 5 (a) Schematic illustration of the stepwise process for the fabrication of the $CsBi_3I_{10}$ perovskite film PD. (b) Comparison of the absorption of the $CsBi_3I_{10}$ film and the photoresponsivity of the $CsBi_3I_{10}$ film-based PD. Reprinted with permission from ref. 84. Copyright 2017 American Chemical Society. (c) Schematic of the preparation process of $MA_3Bi_2I_9$ films and a picture of the as-prepared films on the FTO substrate. (d) The photoresponsivity and D^* plots as a function of different light wavelengths at a fixed intensity of 10 μW cm^{-2} under 0 V. Reprinted with permission from ref. 43. Copyright 2019 Royal Society of Chemistry. (e) Crystal structure of $(1,3\text{-propanediammonium})_2Bi_2I_{10}{\cdot}2H_2O$. Reprinted with permission from ref. 87. Copyright 2019 Royal Society of Chemistry. (f) Typical optical images of the obtained $Cs_3Bi_2I_9$ NPs on different substrates, and the corresponding AFM image of the NPs on the SiO_2/Si substrate. Reprinted with permission from ref. 88. Copyright 2019 Royal Society of Chemistry. (g) Optical image of the $Cs_3Bi_2I_9$ SC thin film. (h) The dynamic-range characterization of the PDs based on $Cs_3Bi_2I_9$ SC thin film at −2 V bias with white LED light illumination of various light intensities. Reprinted with permission from ref. 89. Copyright 2020 WILEY-VCH.

solvent evaporation crystallization method by Kuang and co-workers.[89] The optical image in Fig. 5g presents that a hexagonal shaped crystal with 4 mm in lateral size was obtained. The SC thin film possesses a very low trap density and a high carrier mobility, which are beneficial for their optoelectronic performance and stability. Experimentally, the minimum detection limit of $Cs_3Bi_2I_9$ SC thin film PD is as low as 10^{-4} mW cm^{-2}, a large LDR of 117 dB is obtained (Fig. 5h), and the device exhibits an excellent long-term stability, highlighting their potential applications operated under harsh conditions. In addition to NPs, bulk SCs are also one of the options for achieving high-quality PDs because of their low defect density,[90–95] and different methods have been developed to prepare high-quality SCs. Sun and co-workers demonstrated the growth of $Cs_3Bi_2I_9$ bulk crystals (15×60 mm^3) using a modified vertical Bridgman method, as shown in Fig. 6a.[91] They reported the observation of a resolved energy peak using α particles with a spectral resolution of 32% for the first time. Liu *et al.* developed a nucleation-controlled method to grow centimeter-sized $Cs_3Bi_2I_9$ perovskite SCs, as shown in Fig. 6b.[61] By using this technique, they harvested some large sized SCs with a low trap density and thus the device based on such SCs obtained good performance. Fig. 6c shows the dark current–voltage (I–V) curve of the $Cs_3Bi_2I_9$ SC PD, which exhibits a low dark current of 6 pA at 10 V bias, and the photoresponsivity and D^* are obtained as high as 1.1 A W^{-1} and 4.7×10^{12} jones, respectively, as shown in Fig. 6d and e. In addition, its outstanding thermal stability facilitates the development of a high temperature X-ray detector with stable response at 100 °C. Zhang *et al.* synthesized the $(aminoguanidinium)_3Bi_2I_9$ ($AG_3Bi_2I_9$) bulk SCs with dimensions of up to $24 \times 12 \times 5$ mm^3 by a low-cost evaporation method of the hydroiodic acid aqueous solution, which shows a direct bandgap of about 1.89 eV.[92] As shown in the right panel of Fig. 6f, the bulk SCs can be peeled off through the Scotch tape into slices with an area of up to 0.6 cm^2, which

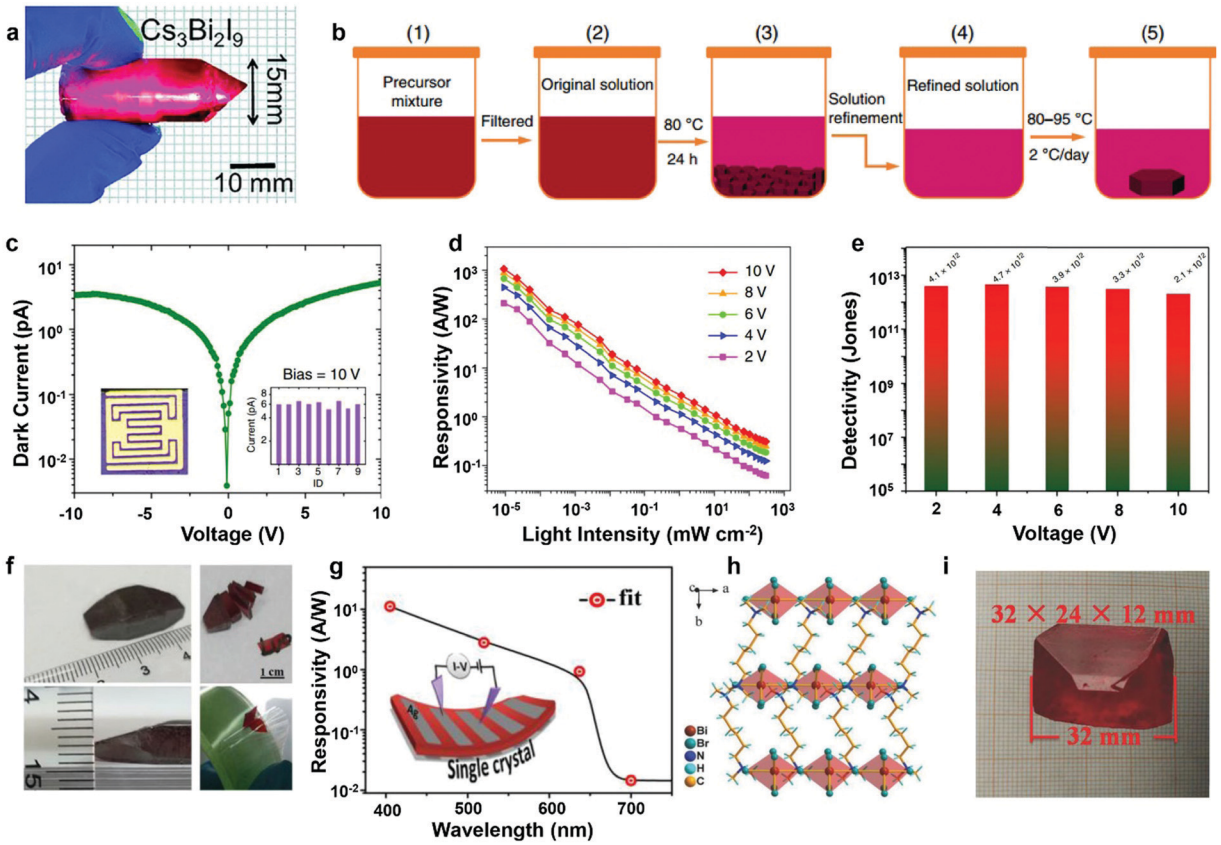

Fig. 6 (a) The $Cs_3Bi_2I_9$ ingot viewed under intense light irradiation. Reprinted with permission from ref. 91. Copyright 2018 Royal Society of Chemistry. (b) Schematic of the nucleation-controlled method to grow $Cs_3Bi_2I_9$ SC. (c) Dark *I*–*V* curve of the Cs3Bi2I9 SC PD (the right-hand inset shows the dark current statistics of different devices, and the left-hand one is the device configuration) (d) Light-intensity-dependent photoresponsivity, and (e) *D** of the $Cs_3Bi_2I_9$ SC PD measured at various biases. Reprinted with permission from ref. 61. Copyright 2020 Nature Publishing Group. (f) Photographs of as-grown $AG_3Bi_2I_9$ SC with size of up to 24 × 12 × 5 mm (left), the ultra-thin wafer, showing brilliant clarity (top right), and flexible exfoliated wafer (bottom right). (g) Wavelength-dependent photoresponsivity under a 405 nm laser with the light intensity of 20 μW cm^{-2} at a 4 V bias. The inset is the schematic of exfoliated $AG_3Bi_2I_9$ SC PD. Reprinted with permission from ref. 92. Copyright 2019 American Chemical Society. (h) Structural packing viewed along the *c*-axis. (i) Photograph of a bulk SC of (TMHD)$BiBr_5$. Reprinted with permission from ref. 93. Copyright 2018 WILEY-VCH.

lays the foundation for realizing low-defect flexible optoelectronic applications. The schematic illustration of flexible exfoliated wafer-based planar detectors is shown in Fig. 6g, and excellent photodetection ability was realized. In addition to PDs based on the $A_3Bi_2X_9$ structure, bulk SC PDs based on other structures have also been demonstrated. For example, by a facile solution process, Luo *et al.* reported a new (TMHD)$BiBr_5$ (TMHD = *N*,*N*,*N*,*N*-tetramethyl-1,6-hexanediammonium) perovskite.[93] The structural analysis reveals that it crystallizes in the monoclinic system with a space group of *P*21/*c* at room temperature, as illustrated in Fig. 6h. Emphatically, high-quality SCs with the dimensions of 2 × 24 × 12 mm^3 are successfully grown (Fig. 6i). PDs based on bulk lead-free (TMHD)$BiBr_5$ SCs were prepared, which show a rapid response speed of 8.9/10.2 ms. The results highlight that the (TMHD)$BiBr_5$ bulk SCs can serve as promising candidates for photodetection.

3.2.2. Sb-based halide perovskites. Although antimony-containing films and anti-solvent vapor-assisted bulk crystals of $MA_3Sb_2I_9$, $(NH_4)_3Sb_2I_xBr_{9-x}$, and $Cs_3Sb_2I_9$ perovskites have been prepared since 2015, Sb-based perovskite PDs were not intensively studied.[96–98] In recent years, Sb-based perovskites with micro/nano-structures, such as NWs, nanoflakes (NFs), and SCs, have been employed for photodetection studies. Pradhan *et al.* first demonstrated the fabrication of PDs using the $Cs_3Sb_2Cl_9$ perovskite NWs as the light absorber.[44] By using the colloidal synthesis route, they synthesized micron-long $Cs_3Sb_2Cl_9$ NWs and nanorods. The *I*–*V* characteristics of the fabricated device show the detection behavior under visible light, as shown in Fig. 7a, and the inset shows the corresponding optical image. The device performance of $Cs_3Sb_2Cl_9$ NW PDs is remarkable in terms of a large photoresponsivity of ~3616 A W^{-1}. Even so, the ability of such PDs to detect weak light needs to be improved because of a relatively low *D** of 1.25 × 10^6 jones. Then, an inverse temperature crystallization method was developed by Zheng and co-workers to grow a large size of ~100 μm $Cs_3Sb_2Br_9$ perovskite NFs, as seen in Fig. 7b.[99] Different sizes of NFs can be synthesized by adjusting the evaporating temperature and solute concentration. In this case, the fabricated $Cs_3Sb_2Br_9$ NF PDs demonstrated an excellent *D** of 2.6 × 10^{12} jones, as displayed in Fig. 7c. In addition, by

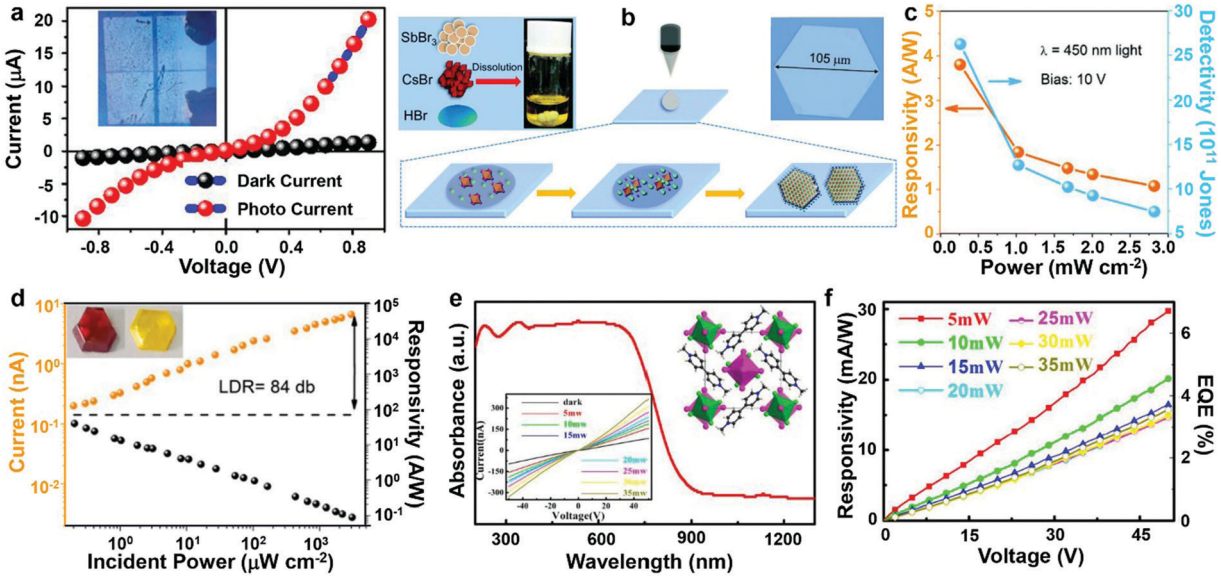

Fig. 7 (a) *I–V* characteristics of $Cs_3Sb_2Cl_9$ NWs PD in the dark and under illumination. The inset shows the optical image of the device. Reprinted with permission from ref. 44. Copyright 2018 American Chemical Society. (b) Middle pattern shows the schematically illustrated growth process of $Cs_3Sb_2Br_9$ perovskite NFs. Right pattern is the optical images of $Cs_3Sb_2Br_9$ perovskite NFs grown on quartz substrates. (c) Power-dependent photoresponsivity and *D** curves under 450 nm light illumination. Reprinted with permission from ref. 99. Copyright 2019 Royal Society of Chemistry. (d) Power-dependent photocurrent and photoresponsivity at a bias of 5 V (460 nm). The inset shows the photographs of the as-prepared $MA_3Sb_2I_9$ (dark red) and $MA_3Sb_2Br_9$ (light yellow) SCs. Reprinted with permission from ref. 100. Copyright 2018 American Chemical Society. (e) Absorption of the (MV)$[SbI_3Cl_2]$. The insets show the *I–V* curves of (MV)$[SbI_3Cl_2]$ PD in the dark and under different light illumination and the general view of (MV)$[SbI_3Cl_2]$ perpendicular to the *c*-axis. (f) Responsivities and EQEs of the fabricated devices. Reprinted with permission from ref. 101. Copyright 2020 American Chemical Society.

employing the $MA_3Sb_2I_9$ micro-single crystals (MSCs) as the active material, which are characterized by a low trap state density of $\sim 10^{10}$ cm^{-3} and a long carrier diffusion length reaching 3.0 μm,[100] Yang and co-workers developed a high-performance PD. As shown in Fig. 7d, the photoresponsivity and *D** of $MA_3Sb_2I_9$ MSC PD are as high as 40 A W^{-1} and $\sim 10^{12}$ jones, respectively. In particular, the PDs exhibit a fast response time (<1 ms) to monochromatic light (460 nm) illumination. Similarly, except for the $A_3Sb_2X_9$ structure, PDs based on other structures have also been demonstrated. Very recently, Lei *et al.* synthesized (MV)$[SbI_3Cl_2]$ SC (MV^{2+}; *N*,*N*′-dimethyl-4,4′-dipyridylium) by a solvothermal method, which has 1D inorganic frameworks of the I-sharing double octahedra. The (MV)$[SbI_3Cl_2]$ possesses a direct bandgap of 1.5 eV (Fig. 7e), and shows an obvious photoresponse to visible light.[101] Under 532 nm illumination with the power of 5 mW at a bias of 50 V, the photoresponsivity and EQE are 29.75 mA W^{-1} and 6.69%, respectively (Fig. 7f). The (MV)$[SbI_3Cl_2]$ will provide an alternative material for photodetector applications.

3.2.3. Lead-free double perovskites. Lead-free double perovskites are considered to be promising alternatives for lead-based perovskites due to their remarkable optoelectronic properties and significantly enhanced chemical and thermodynamic stability. Since 2017, many studies have been carried out to evaluate the photodetection performance of lead-free double perovskites targeted at visible light and X-rays.[102–113] In this part, we mainly focus on the progress of PDs in visible light, and the X-ray detectors based on lead-free double perovskites will be discussed later. Greul *et al.* first demonstrated the preparation of $Cs_2AgBiBr_6$ films by a solution method. As shown in Fig. 8a, the surface coverage and film quality are improved by preheating the precursor and substrate to 75 °C before spin coating.[114] By using the same synthesis method, Lei *et al.* firstly reported a photoconductive-type PD by using the $Cs_2AgBiBr_6$ films as the light absorber.[103] Li and co-workers also reported a $Cs_2AgBiBr_6$-based self-powered PD based on the above methods.[65] In their case, the $Cs_2AgBiBr_6$ light absorber is characterized by the high-density and low-size nanocrystallites, which are short of well-defined facets and irregularly stacked. As a result, the undesired trap states may exist at the interfacial areas among the nanocrystallites, and a poor photodetection ability can be expected. To overcome this problem, Yang *et al.* optimized the synthesis method, and high-quality $Cs_2AgBiBr_6$ films with large grain sizes, long charge carrier lifetimes, and low trap densities were obtained.[107] Correspondingly, an optimized multilayer heterojunction device (including optimized hole- and electron-transporting layers) was prepared, which shows a remarkable performance (Fig. 8b and c). More importantly, due to the low defect densities and multilayer heterojunction device structure, the $Cs_2AgBiBr_6$ perovskite-based PDs exhibit a superior operational stability. For the non-encapsulated devices, there is almost no degradation in the PD performance under a high temperature of 150 °C, and ~94% of the initial photoresponsivity can be retained after storage in ambient air for 2300 h. In addition, high-quality $Cs_2AgBiBr_6$ films can also be prepared by modifying the substrate surface with an ultrathin metal oxide (MO_x) layer.[111] Fig. 8d shows the schematic diagram of the formation of Bi–O bonds at the interface between the

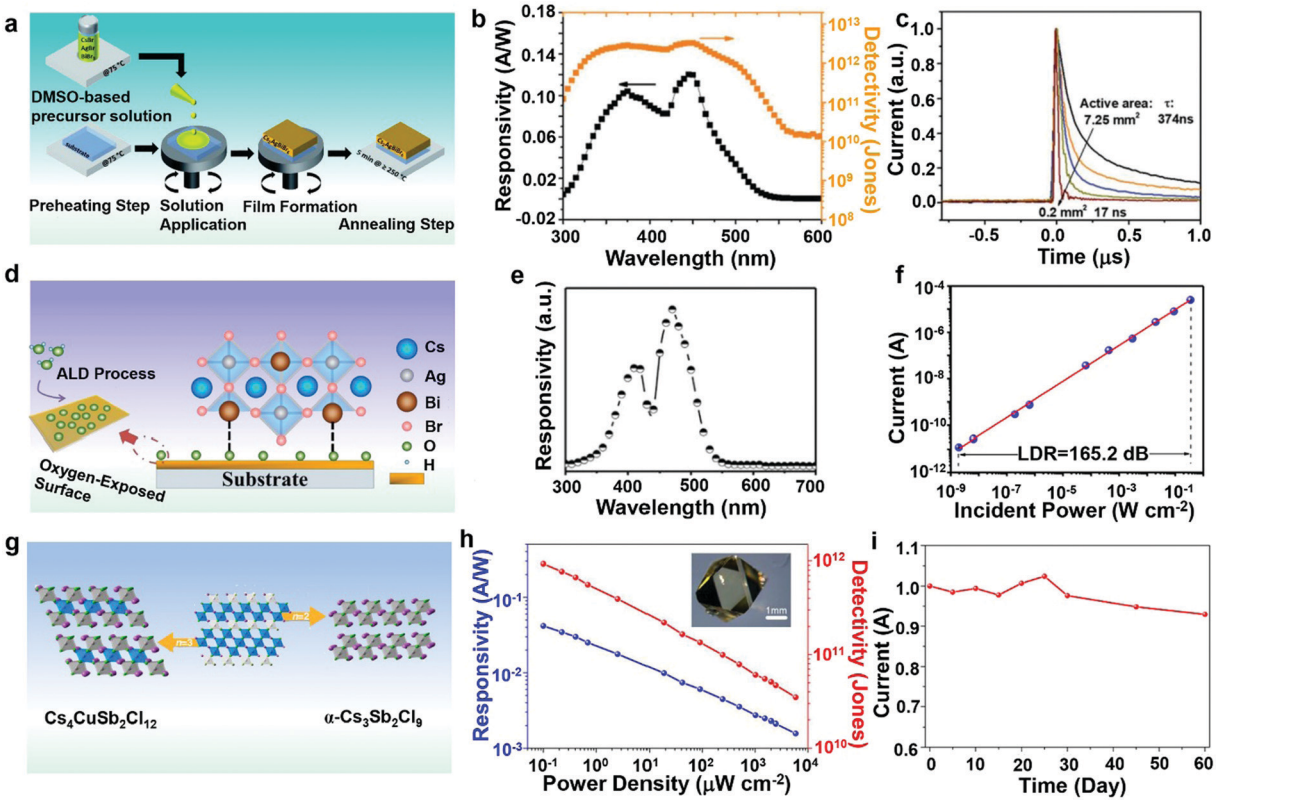

Fig. 8 (a) Schematic of the synthesis route for $Cs_2AgBiBr_6$ films. Reprinted with permission from ref. 114. Copyright 2017 Royal Society of Chemistry. (b) Photoresponsivity and D^* of the $Cs_2AgBiBr_6$ PDs at 0 V. (c) Transient photocurrent at 0 V bias of the $Cs_2AgBiBr_6$ PDs with different active areas from 7.25 to 0.2 mm^2. Reprinted with permission from ref. 107. Copyright 2019 WILEY-VCH. (d) Schematic diagram of the Bi–O interfacial interaction at the ALD-MO_x layer-modified substrate/$Cs_2AgBiBr_6$ interface. (e) Normalized spectral photoresponsivity of the PD. (f) LDR of the device. Reprinted with permission from ref. 111. Copyright 2020 American Chemical Society. (g) Family of [111]-oriented perovskites with general formula: $A_{n+1}B_nX_{3n+3}$, which can be obtained by cutting along the [111]-direction of the 3D parent structure. Panels A and B show the crystal structures of $Cs_4CuSb_2Cl_{12}$ and α-$Cs_3Sb_2Cl_9$. Cl and Cs atoms are depicted as green and purple spheres, respectively; Sb and Cu coordination polyhedra are shown in gray and blue, respectively. Reprinted with permission from ref. 115. Copyright 2017 American Chemical Society. (h) The inset is a picture of the Cs2AgInCl6 SC. Light intensity-dependent photoresponsivity and normalized D^* under a bias of 5 V under vacuum. (i) Storage stability of $Cs_2AgInCl_6$ PDs. Reprinted with permission from ref. 45. Copyright 2018 American Chemical Society.

substrate and $Cs_2AgBiBr_6$ films. The Bi atoms in $Cs_2AgBiBr_6$ lattices would bond with the oxygen atoms on the substrate surface, leading to the improvement of the film quality and photoelectric performance. Fig. 8e shows the spectral response characteristic of the device, which exhibits a remarkable photoresponsivity ranging from 350 to 550 nm, and a large LDR of 165.2 dB (Fig. 8f). Although great efforts have been made to improve the performance of $Cs_2AgBiBr_6$-based PDs, their indirect bandgap characteristics reduce its potential for PD applications. That is, a much thicker absorbing layer is necessary for indirect bandgap materials due to the weak oscillator abilities for either light absorption or radiative recombination. To solve this problem, some studies have been performed to explore other lead-free double perovskites with a direct bandgap.[46,115–120] For example, lead-free double perovskite $Cs_4CuSb_2Cl_{12}$ microcrystallite with direct bandgap was fabricated and studied by Batabyal *et al.*[46] $Cs_4CuSb_2Cl_{12}$ is a triple layered perovskite formed by interlocking octahedrons of Sb^{3+} and Cu^{2+}. It has a structure similar to $Cs_3Sb_2Cl_9$, which can be thought of as having a $CuCl_6$ octahedron sandwiched between layers of $SnCl_6$ (Fig. 8g).[115] Except for the film-based PDs, LFHP SCs were also synthesized and applied. Tang and co-workers prepared high-quality $Cs_2AgInCl_6$ SCs by the hydrothermal method.[45] The inset of Fig. 8h shows the photograph of corresponding $Cs_2AgInCl_6$ SCs, which possesses truncated octahedral shape with an average size of 2.88 mm × 2.81 mm × 1.95 mm and smooth surfaces. Then, UV detectors with a photoconductive planar structure were fabricated, demonstrating a fast response time of ~1 ms, and a high D^* of 10^{12} jones. Moreover, the studied PD is very stable, and maintained 90% of the initial device performance after storage in ambient conditions (~25 °C, and 55% relative humidity) for 60 days, as seen in Fig. 8i, indicating its advantages for optoelectronic applications.

3.3. Perovskite derivatives

Recently, another family of ternary perovskite derivatives has also been intensively studied for PDs. Currently, there are three main synthesis approaches for perovskite derivatives, including spin-coating,[121–125] the modified anti-solvent vapor-assisted

crystallization process,[126] and vacuum-based deposition.[127] Fig. 9a shows the schematic illustrations of the spin-coating process for the preparation of copper halide $Cs_3Cu_2I_5$ films,[122] and the process can be described as dropping anti-solvent near the end of the spin-coating process to accelerate crystallization. By using this method, Li *et al.* reported a spectral-selective PD based on the $Cs_3Cu_2I_5$ films. The surface-charge recombination can be controlled through the thickness of the absorber and the device responds only to photons with an energy in a narrow "window" of 300–370 nm.[121] Also, by a modified anti-solvent vapor-assisted crystallization method, Zhang *et al.* realized a sensitive deep-UV PD with $Cs_3Cu_2I_5$ crystalline films as the active layer,[126] exhibiting remarkable sensitivity to deep UV light with the photoresponsivity of 64.9 mA W^{-1}. In addition to the solution method, vacuum evaporation can also be used for thin film preparation, and the corresponding schematic preparation is shown in Fig. 9b. Lately, Tang *et al.* prepared $CsCu_2I_3$ films by the vacuum thermal evaporation method.[127] Compared with the solution-phase method, the vacuum evaporation technique can achieve a high surface coverage for the $CsCu_2I_3$ films composed of small nano-grains, which are more advantageous in device construction.

Except for the film-based PDs, devices based on perovskite derivative SCs have also been studied. In 2018, Jun *et al.*

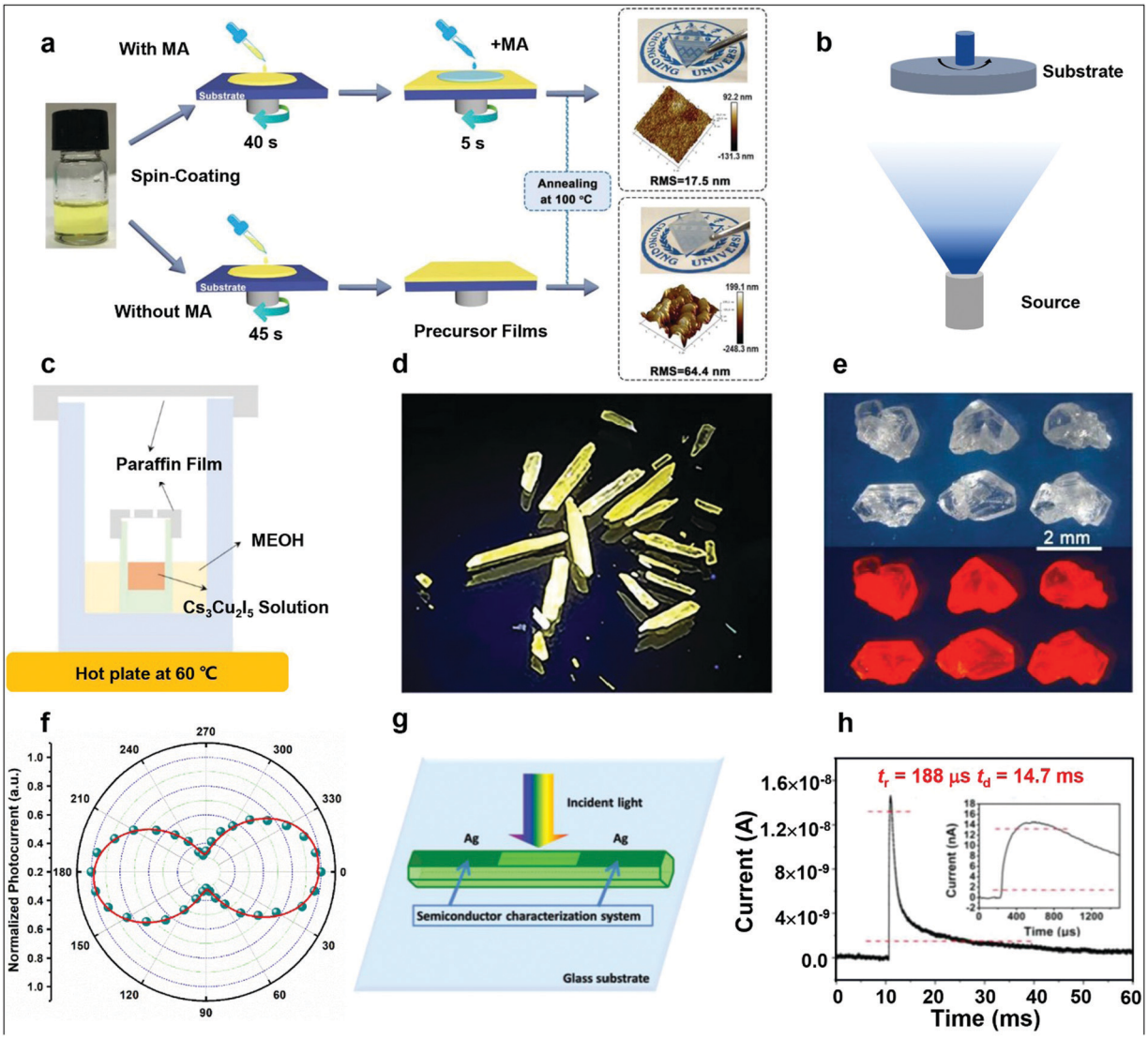

Fig. 9 (a) Schematic illustration of the spin-coating procedure with/without MA in the fabrication of $Cs_3Cu_2I_5$ films, and the photographs and 3D AFM images of the as-prepared films on ITO substrate. Reprinted with permission from ref. 122. Copyright 2020 Elsevier. (b) Vacuum thermal evaporation system for depositing the perovskite absorbers. (c) Schematic of anti-solvent vapor-assisted crystallization of $Cs_3Cu_2I_5$ SCs. Reprinted with permission from ref. 128. Copyright 2018 WILEY-VCH. (d) Optical images of 1D $CsCu_2I_3$ crystals. Reprinted with permission from ref. 130. Copyright 2019 WILEY-VCH. (e) Images of $Cs_2InBr_5{\cdot}H_2O$ SC under ambient light (top) and UV light (bottom). Reprinted with permission from ref. 134. Copyright 2019 WILEY-VCH. (f) Polarization-dependence of the photocurrent for $CsCu_2I_3$ NWs with a width of 600 nm. Reprinted with permission from ref. 131. Copyright 2020 Royal Society of Chemistry. (g) Schematic diagram of the $CsCu_2I_3$ PD. (h) Estimated t_r and t_d from the single pulse response curve; the inset is the enlarged curve. Reprinted with permission from ref. 132. Copyright 2020 WILEY-VCH.

synthesized $Cs_3Cu_2I_5$ SCs by the anti-solvent vapor-assisted crystallization method.[128] As seen in Fig. 9c, the $Cs_3Cu_2I_5$ precursors were placed in a bottle and covered with a paraffin film with a small hole. The covered bottle was placed inside a beaker filled with methanol. Then, this beaker was sealed by a paraffin film. In their case, the paraffin film was used to balance the anti-solvent atmosphere and protect the condensing anti-solvent. Note that this method was widely used to synthesize Cu-based, In-based and other perovskite derivatives.[128–130] Fig. 9d shows the optical images of 1D $CsCu_2I_3$ SC synthesized by the above method.[130] The SC is of high quality with a size of about 10 mm × 1.5 mm, and has a strong white-light emission under UV light excitation. Li *et al.* prepared 1D $CsCu_2I_3$ NWs using the same method,[131] and further the NWs were used as the light absorber to fabricate a polarization-sensitive UV PD because of their electric and optical anisotropy of the asymmetric structure and external morphology anisotropy, and a high photocurrent anisotropy ratio of 3.16 was achieved, as shown in Fig. 9f. Due to the high crystallinity and low-dimensional structure of the $CsCu_2I_3$ NWs, the PDs exhibit an excellent photodetection ability. More recently, by a low-cost anti-solvent vapor assisted method, a highly crystalline and highly stable $CsCu_2I_3$ SC was synthesized, and further a high-speed PD with the response speed of t_r/t_d = 0.19/14.7 ms was constructed, as shown in Fig. 9g and h.[132] At the same time, Zhou *et al.* synthesized the $Cs_2InBr_5{\cdot}H_2O$ SC by a low-temperature crystallization method, which is another common method for synthesizing perovskite SCs.[133–135] As shown in Fig. 9e, the optical images of $Cs_2InBr_5{\cdot}H_2O$ SC possess a large size of 2 mm. Similarly, Zhou *et al.* explored the synthesis of copper halide salt $K_2Cu_2Cl_6$ for photodetection applications,[47] and Tang *et al.* demonstrated the X-ray detector using 1D structured Rb_2CuBr_3 synthesized by low-temperature crystallization.[133] The above results motivate the development of high-performance PDs based on nontoxic and stable low-dimensional metal halides in the future.

4. Applications of LFHPs and perovskite derivative PDs

4.1. Biological synapses

It is possible to store and process information at the same time by adjusting the connection between two adjacent neurons, that is, biological synapses. Recently, many artificial synaptic devices have been developed based on the above principles.[143–146] In the light synapse devices, the light pulse is regarded as a presynaptic stimulus, and the current is the synaptic weight. Light pulses can be transmitted to the device by generating excitatory postsynaptic current (EPSC). Using the relatively long decay time (0.63/3.6 s) caused by Sn-cation vacancies and the concept of biological synapses, Qian *et al.* applied 2D lead-free perovskite $(PEA)_2SnI_4$ films in light controlled memory devices.[79] Fig. 10a shows

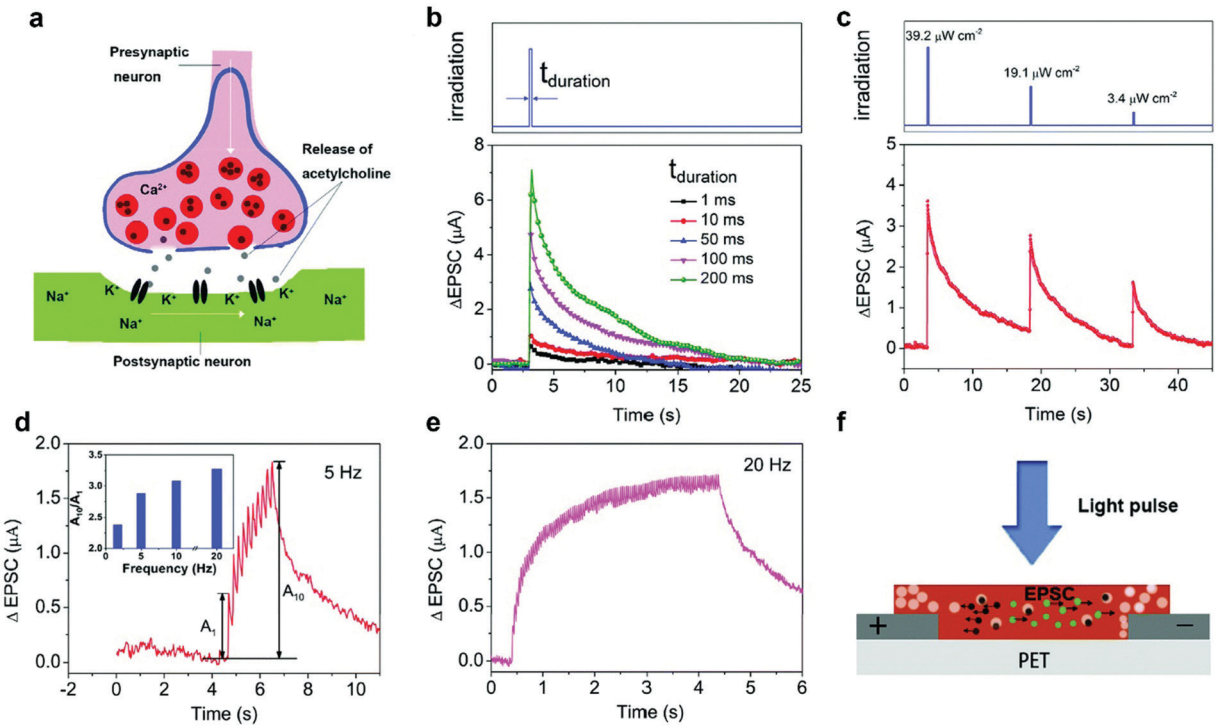

Fig. 10 (a) Schematic illustration of a biological synapse. (b) ΔEPSC under 470 nm light excitation with different pulse durations (40 μW cm^{-2} irradiance). (c) ΔEPSC under several 470 nm light pulses with the same duration time (10 ms) and different irradiance (39.2, 19.1, and 3.4 μW cm^{-2}). (d) ΔEPSC under 10 light pulses with a time interval of 200 ms (including 10 ms duration time). The inset is the histogram of frequency-dependent EPSC gain (A_{10}/A_1). (e) ΔEPSC under 100 light pulses with a time interval of 50 ms (including 10 ms duration time). (f) The scheme for the working mechanism of the 2D perovskite-based synaptic device (white balls for vacancies; black balls for electrons; green balls for holes). Reprinted with permission from ref. 79. Copyright 2018 Royal Society of Chemistry.

the schematic diagram of a biological synapse. The EPSC increases from 0.8 to 7.0 μA as the light pulse duration time increases from 1 to 200 ms, as shown in Fig. 10b. Then, a series of light pulses with different light intensities and the same duration time of 10 ms was applied on the device, and ΔEPSC decreased from 3.7 to 1.7 μA with decreasing irradiance, as shown in Fig. 10c. The above results are quite similar to those in a biological excitatory synapse. The dynamic synaptic behaviors of the device were also studied. As seen in Fig. 10d, when the device was stimulated by multiple light pulses, the peak value of EPSC gradually increased. After turning off the light, the EPSC decreased to the original current. This is similar to the short-term plasticity of a biological excitatory synapse. This work suggests that Sn-based perovskites can be used in light controlled memory devices, which can simulate the short-term plasticity of biological synapses due to the existence of Sn vacancies.

4.2. Imaging applications

Image sensors are widely used in digital cameras, industry, and defense.[147,148] In recent years, research on imaging capabilities based on perovskites has been extensively carried out, and image sensors based on different wavelengths have been successfully realized. For example, UV imaging applications were demonstrated by deploying the $Cs_3Cu_2I_5$/GaN heterojunction PD as the sensing pixels.[121] Fig. 11a displays the high-resolution results of the hollow "UV" logo and a solid symbol of a deer under UV light illumination, indicating the high fidelity features of the imaging system and the reliable imaging function of the device. Zhu *et al.* realized the integration of a 6 × 6 pixel array based on the Sn-rich binary perovskite devices for visible imaging applications.[76] They first tested the photocurrent uniformity of these pixels, which is important as the photocurrent difference of every pixel degrades the image quality. As shown in Fig. 11b and c, these 6 × 6 PD pixels show normalized photocurrent from 0.7 to 1.0, which indicates the remarkable photocurrent uniformity. Then, a hollow "+" sign was put between the device and the incident light. As shown in Fig. 11d, the image was recorded vividly, promoting their further development in practical application. Wang *et al.* also realized near-infrared imaging using Sn-rich perovskite PDs and an indium gallium zinc oxide film transistor-matrix backplane.[77] The 12 × 12 array was illuminated with 850 nm infrared light at an intensity of 1374 mW cm^{-2} through an "11" shape shadow mask. The result is shown in Fig. 11e, with a clear shape of number "11" (red frame). Besides, X-ray imaging was also realized by Liu and co-workers.[61] They demonstrated a nucleation-controlled method to grow large-size $Cs_3Bi_2I_9$ SC, in which they reduced the number of crystal nuclei to ensure that each one independently grows. The $Cs_3Bi_2I_9$ SC shows a low trap density, ultra-low dark current noise and high stability, and these characteristics suggested that the $Cs_3Bi_2I_9$ SC would exhibit excellent imaging capability. Fig. 11f shows the schematic of the vertically structured X-ray detector (Au/$Cs_3Bi_2I_9$ SC/Au), and the images of a metallic nut were reproduced by X-ray imaging (Fig. 11g). The clear color contrast demonstrates that these objects were clearly resolved.

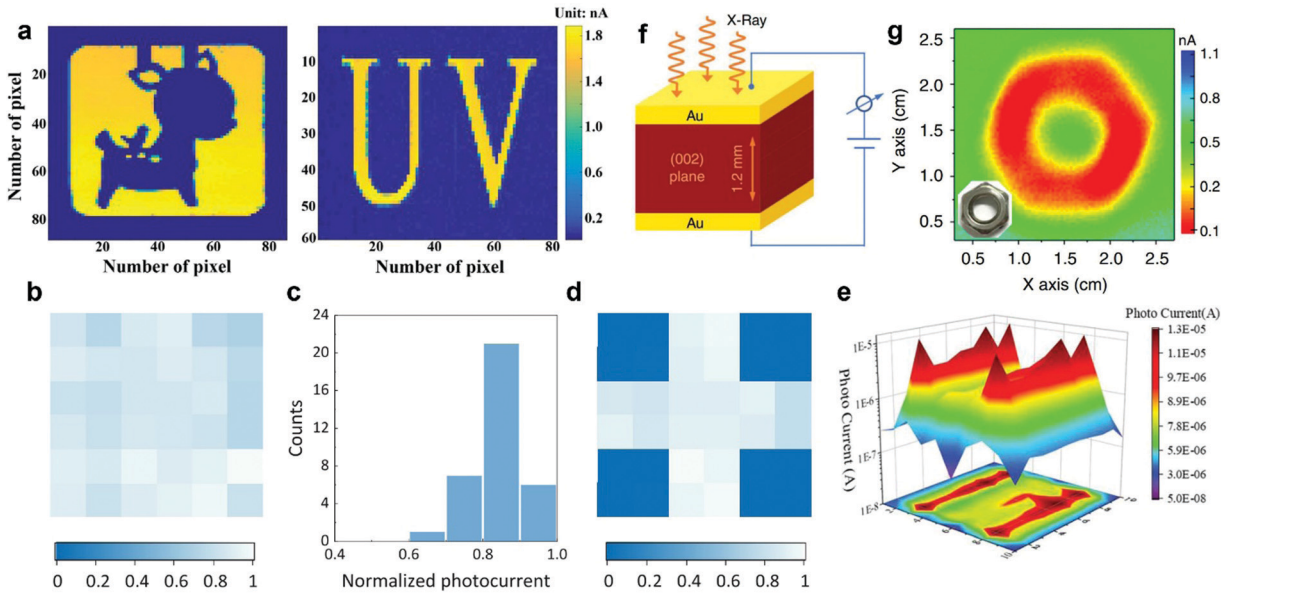

Fig. 11 (a) The current mapping of deer and UV patterns based on the $Cs_3Cu_2I_5$/GaN heterojunction PDs. Reprinted with permission from ref. 121. Copyright 2019 Royal Society of Chemistry. (b) Photocurrent uniformity of 6 × 6 Sn-rich binary PD pixels. (c) Photocurrent distribution of 36 Sn-rich PD pixels. (d) Image of a "+" sign naturally captured by Sn-rich binary PD imaging array with 6 × 6 pixels. Reprinted with permission from ref. 76. Copyright 2019 American Chemical Society. (e) The intensity profile obtained by measuring the photocurrent of the pixels. The number "11" is readily imaged by the device. Reprinted with permission from ref. 77. Copyright 2019 WILEY-VCH. (f) Schematic of the $Cs_3Bi_2I_9$ SC-based X-ray detector structure. (g) Photo and corresponding X-ray image of a nut obtained using the $Cs_3Bi_2I_9$ SC detector (1 × 1 mm^2), as measured under 50 V mm^{-1} electric field with a dose rate of 36.2 μGy_{air} s^{-1}. Reprinted with permission from ref. 61. Copyright 2020 Nature Publishing Group.

4.3. X-Ray detection

The detection of X-ray photons is of utmost importance for a wide range of applications, from specific crystal structure determinations to radio astronomy. Lead-based perovskites have been proven to be suitable materials for X-ray detection, owing to the heavy Pb and halide atoms.[149–151] Considering that Bi is the heaviest stable element, and the X-ray absorption of Bi-based LFHPs and Cs_2AgBiX_6 (X = Cl, Br, and I) double perovskites could be stronger than lead-based counterparts and commercial α-Se X-ray detectors. In 2017, Tang *et al.* first reported $Cs_2AgBiBr_6$ SC X-ray detectors with a low detection limit.[102] They designed and fabricated a vertical device structure of Au/Cs_2AgBiX_6 SC/Au, with a 2 mm-thick $Cs_2AgBiBr_6$ SC as the active material. The optimized device exhibited a high sensitivity of 105 μC Gy_{air}^{-1} cm^{-2} and a low detection limit of 59.7 nGy_{air} s^{-1} under an external bias of 5 V. Thereafter, a series of interesting works were conducted by Tang's group to improve the performance of the Cs_2AgBiX_6 X-ray detector.[106,110] For instance, to inhibit the undesired ionic migration behavior in $Cs_2AgBiBr_6$ polycrystalline wafers, Tang and co-workers introduced bismuth oxybromide (BiOBr) as the hetero-epitaxial passivation layer to passivate the surface defects of $Cs_2AgBiBr_6$, and thus the ionic migration was also effectively suppressed, as illustrated in Fig. 12a.[106] Hence, the detector achieved outstanding balanced performance with a signal drifting by one order of magnitude lower than other studies, a high sensitivity of 250 μC Gy_{air}^{-1} cm^{-2}, and a spatial resolution of 4.9 lp mm^{-1} (Fig. 12b and c). Then, they proposed a solubility and supersolubility guidance scheme applied to $Cs_2AgBiBr_6$ SC growth. As shown in Fig. 12d, compared with the unoptimized ones, the promoted $Cs_2AgBiBr_6$ crystal exhibits a more smooth surface as well as high resistivity with a narrow distribution from 6.1 × 10^9 to 3.31 × 10^{10} Ω cm, leading to an excellently performing X-ray detector with enhanced sensitivity of 1974 μC Gy_{air}^{-1} cm^{-2}.

In 2018, Sun and co-workers reported the growth of $Cs_3Bi_2I_9$ SC using a modified vertical Bridgman method.[91] The $Cs_3Bi_2I_9$ SCs were cut into appropriate sizes along different crystal orientations for optical and electrical anisotropic property studies. The X-ray

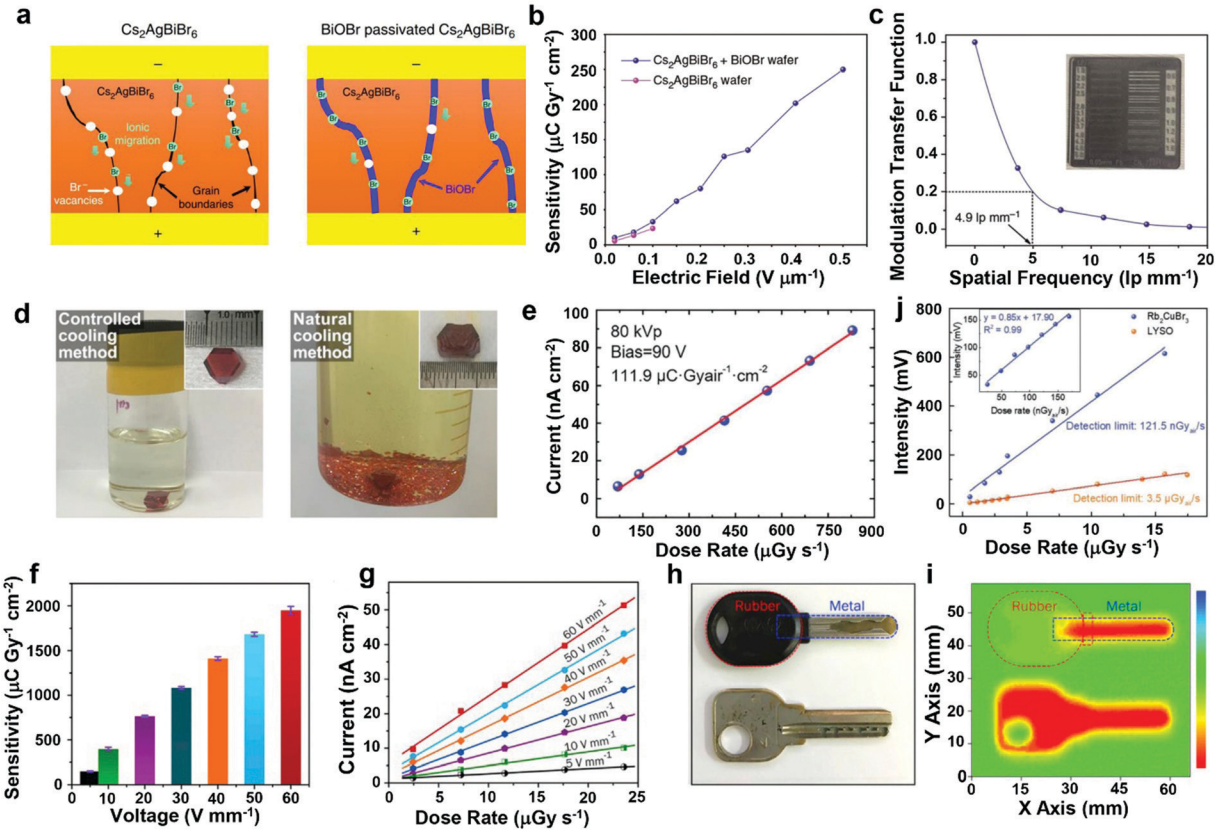

Fig. 12 (a) Schematic illustration of the suppressed ionic migrations by BiOBr passivation. (b) X-Ray sensitivity under different electric fields. (c) Modulation transfer function for the fabricated detector and the inset is the line pair card for edge-spread function measurement. Reprinted with permission from ref. 106. Copyright 2019 Nature Publishing Group. (d) The resulting solution and crystals synthesized by a controlled cooling method and natural cooling method. The insets show the synthesized crystals. Reprinted with permission from ref. 110. Copyright 2019 WILEY-VCH. (e) X-Ray photocurrent as a function of exposure dose rate based on the device of Au/$Cs_3Bi_2I_9$ SC/Au. Reprinted with permission from ref. 91. Copyright 2018 Royal Society of Chemistry. (f) X-Ray sensitivity of the $MA_3Bi_2I_9$ SC detector as a function of applied electric field. (g) X-Ray response current at various dose rates (the sensitivity can be derived from the slope of the fitting line). (h) Photographs, and (i) corresponding X-ray images of a metallic key with partial wrapping in rubber and a naked metal key, respectively. The dose rate for imaging is 23.57 μGy_{air} s^{-1} and the electric field is 60 V mm^{-1}. Reprinted with permission from ref. 95. Copyright 2020 Cell Press. (j) Emission intensity of Rb_2CuBr_3 as a linear function of dose rate. The inset is the data of Rb_2CuBr_3 below 200 nGy_{air} s^{-1} for detection limit measurement. Reprinted with permission from ref. 133. Copyright 2019 WILEY-VCH.

Table 2 Summary of the lead-free metal halide X-ray detectors

Materials	Detection sensitivity ($\mu C\ Gy_{air}^{-1}\ cm^{-2}$)	Detection limit ($nGy_{air}^{-1}\ s^{-1}$)	Electric field ($V\ mm^{-1}$)	Ref.
$Rb_3Bi_2I_9$ SC	159.7	8.32	300	94
$Cs_3Bi_2I_9$ SC	111.9	—	450	92
$MA_3Bi_2I_9$ SC	1947	83	60	95
$MA_3Bi_2I_9$ SC	872	31	286	152
$MA_3Bi_2I_9$ polycrystalline pellets	563	9.3	200	153
$Cs_3Bi_2I_9$ SC	1652.3	130	50	61
$Cs_2AgBiBr_6$ SC	105	59.7	25	102
$Cs_2AgBiBr_6$ SC	288.8	—	22.7	105
$Cs_2AgBiBr_6$ SC	250	95.3	500	106
$(BA)_2Cs_2AgBiBr_7$ SC	4.2	—	—	108
$Cs_2AgBiBr_6$ SC	1974	45.7	50	110
Rb_2CuBr_3 SC rod	—	121.5	—	133

response of a 2 mm $Cs_3Bi_2I_9$ SC detector was explored using a tungsten X-ray source. According to the relationship $S = (I_{ON} - I_{OFF})$/dose rate, a high X-ray sensitivity of 111.9 $\mu C\ Gy_{air}^{-1}\ cm^{-2}$ was obtained, as shown in Fig. 12e. In addition, organic–inorganic hybrid $MA_3Bi_2I_9$ SC was also synthesized by Liu and co-workers to achieve the X-ray detection.[92,95] They first reported the inch-sized ($26 \times 26 \times 8\ mm^3$) 0D $MA_3Bi_2I_9$ SC using a precursor refinement strategy to remove the superfluous nucleation seeds. These crystals have significantly lower ion migration, reduced dark current, and better environmental stability compared with other lead-halide perovskites. The resulting devices show a surprisingly high sensitivity of 1947 $\mu C\ Gy_{air}^{-1}\ cm^{-2}$ at a bias of 60 V mm^{-1}, and a very low detection limit of 83 $nGy_{air}\ s^{-1}$, as shown in Fig. 12f and g. Furthermore, they designed an X-ray imaging system based on this 0D-structured $MA_3Bi_2I_9$ SC. To demonstrate the capability of the imaging system to resolve small features, they scanned two metallic keys by a device (Fig. 12h). It should be noted that the metal parts inside the rubber can also be clearly shown by the obvious contrast in the X-ray imaging, indicating that the unique function of X-ray imaging is the ability to penetrate materials, which are opaque to visible light, as seen in Fig. 12i. Except for Bi-based LFHPs and Cs_2AgBiX_6 (X = Cl, Br, and I) double perovskites, Rb_2CuBr_3 was also a good candidate for sensitive X-ray detection.[133] The high PL quantum yield of Rb_2CuBr_3 combined with strong X-ray absorption capability enables a record high light yield of ~91 056 photons per MeV among perovskites and relative scintillators, and the detection limit of Rb_2CuBr_3 is 121.5 $nGy_{air}\ s^{-1}$, as shown in Fig. 12j. The above results indicate the strong competitiveness of lead-free metal halides in the next generation of X-ray imaging, and the device performance parameters obtained from some representative literature are summarized in Table 2.

5. Conclusion and outlook

In summary, we have reviewed the currently explored LFHPs and perovskite derivatives, and discussed their structures, synthesis and modification methods, optoelectronic properties, and photodetection applications. As potential photo-active materials, their preliminary applications in PDs are encouraging, with potential for cost-effective and large-scale manufacturing from abundant materials.

Firstly, replacing Pb with Sn, Ge is an attractive option, and the resulting $CsSnX_3$ and $CsGeX_3$ are comparable with lead-based perovskites or even better in some aspects. However, the easy oxidation of Sn^{2+} to Sn^{4+} represents a large concern for their stability. Substitution of Sn^{2+} with more stable Sn^{4+} has been adopted as an attractive option, and A_2SnX_6 (X = Cl, Br, and I)-based PDs have been demonstrated. Secondly, Bi^{3+}- and Sb^{3+}-based perovskites are recognized as one of the most promising candidates among LFHPs and perovskite derivatives due to the similar ns^2 electronic configuration with Pb. By now, a series of Bi^{3+}- and Sb^{3+}-based perovskites with structures of $A_3Bi_2X_9$, ABi_3X_{10}, and $A_3Sb_2X_9$ ($A = MA^+$, FA^+, Rb^+, and Cs^+; $X = I^-$, Br^-, and Cl^-) have been developed experimentally, and photodetection applications were also demonstrated. However, the replacement of Pb by Sb or Bi would reduce the dimensions of the perovskite structures, leading to reduced band dispersion, increased effective masses of charge carriers, and decreased carrier mobility, which is not conductive to the photoresponse ability of the resulting PDs. Under these circumstances, double perovskites with B-site substitution by mixed cations (B = B(I), and B′ = B(III)) have recently been explored to form 3D LFHPs ($A_2BB'X_6$). Due to the distinguished stability and tunable optical properties, lead-free double perovskites have enormous potential for constructing high-performance, stable and environment-friendly optoelectronic devices for practical applications. Besides, another family of Cu-based perovskite derivatives has been reported recently, which refers to metal halides without clear relation to the perovskite structures. By now, many types of metal halides with different structures have been studied, such as $K_2Cu_2Cl_6$, Rb_2CuBr_3, $Cs_3Cu_2I_5$, and $CsCu_2I_3$, and their future applications in the manufacture of optoelectronics are worthy of expectation.

Through first-principles calculations, the LFHPs and perovskite derivatives show good dynamic stability and thermodynamic stability. Experimentally, the fabricated PDs demonstrate good stability operating in the air, which makes it less demanding on packaging in future applications. In addition, the emerging LFHPs and perovskite derivatives can extend the

response range of Pb-based perovskite PDs, which is a good supplement for practical applications in some special situations. Generally, PDs based on lead-based perovskites can achieve a response range of 300–800 nm. While the Cu-based halides are always characterized by a relatively large bandgap and can realize a deep UV photodetection below 250 nm, Sn-based LFHPs have a smaller bandgap compared with the lead-halide perovskites, and their photoresponse range can extend to the near-infrared region (800–1000 nm).

Although these results are encouraging, the LFHPs and perovskite derivative-based PDs are still far from the requirements for practical applications. Perovskite materials have some inherent limitations on practical application and commercialization. For example, the localized defect states in perovskite lattices and the bulk are harmful for their applications. To solve these problems, detailed studies on the charge carrier dynamics are needed to provide thoughtful concepts for understanding the mechanism of defect traps in the structure. On this basis, more theoretical and empirical investigations are needed to promote the overall performance of LFHP PDs.

(1) Defects in perovskites are still a problem to be solved. Further research should focus on the defect passivation and the growth of high-quality LFHP crystals. Preparation methods, such as solvent engineering or various vapor deposition methods, should be further studied. On the basis of the existing methods, further improving the crystal growth process to obtain perfect lattice LFHPs or introduction of some effective dopants into LFHPs will be beneficial to reduce their trap states.

(2) Though great progress has been made in the synthesis of the LFHPs and perovskite derivatives, highly effective synthesis of crystals with precise shape and size control compared to that of conventional lead-halide semiconductors still urgently needs to be explored. Moreover, the applications of most LFHPs and perovskite derivatives (such as Cu(I)-based metal halides) have not been fully developed, and their unique photophysical properties have not yet been extensively studied, which are significant for various potential applications. Thus, more theoretical and empirical investigations are needed to promote the overall performance of the LFHPs and perovskite derivatives.

(3) The performance of the PDs needs to be further improved. On the basis of highly-crystalline LFHPs, many methods can be used to further improve the device performance. Firstly, the dark current of the PDs can be suppressed by doping or surface modification of LFHPs, which is conductive to obtain a high on/off current ratio. Secondly, to further improve the photoresponsivity of the PDs, the light absorption of the LFHPs should be enhanced, and introducing the plasmon effect into the device may be a good choice. Thirdly, optimizing the device structure is also an important option. For example, the use of photomultiplication mechanisms in PDs could achieve an EQE greater than 100%; thus the ability of the PDs to detect a weak light signal can be improved.

(4) The inevitable stability issue is still the focus of devices in the future. Although perovskite derivatives have been proved to have better stability than the lead-based perovskites in theory and experiment, they are still far from enough for practical applications. The construction of multi-layer heterostructures or the combination with inorganic materials may be a feasible method to improve the stability of the device.

(5) For further development, it is necessary to reduce the size of the devices and improve their integration to achieve practical applications. At the same time, new design strategies are urgently required to synthesize new LFHPs with intriguing physical and optoelectronic properties toward specified applications.

Author contributions

Z. S., X. L. and X. F. provided the conceptualization. Y. L., W. L., J. M., X. C. and D. W. performed the literature review and summary. Y. T. and C. S. carried out the methodology. Y. L. wrote the original draft. Z. S. and X. F. edited the article. Z. S. and X. L. provided the funding support.

Conflicts of interest

There are no conflicts to declare.

Acknowledgements

This work was supported by the National Natural Science Foundation of China (No. 11774318, 12074347, and 61935009) and the Support Program for Scientific and Technological Innovation Talents of Higher Education in Henan Province (19HASTIT017).

Notes and references

1 A. Kojima, K. Teshima, Y. Shirai and T. Miyasaka, *J. Am. Chem. Soc.*, 2009, **131**, 6050–6051.
2 J. Liang, C. X. Wang, Y. R. Wang, Z. R. Xu, Z. P. Lu, Y. Ma, H. F. Zhu, Y. Hu, C. C. Xiao, X. Yi, G. Y. Zhu, H. L. Lv, L. B. Ma, T. Chen, Z. X. Tie, Z. Jin and J. Liu, *J. Am. Chem. Soc.*, 2016, **138**, 15829–15832.
3 M. M. Lee, J. Teuscher, T. Miyasaka, T. N. Murakami and H. J. Snaith, *Science*, 2012, **338**, 643–647.
4 https://www.nrel.gov/pv/assets/pdfs/best-research-cell-efficiencies.20200128.
5 P. Lu, J. Wu, X. Shen, X. Gao, Z. Shi, M. Lu, W. Yu and Y. Zhang, *Adv. Sci.*, 2020, **7**, 2001562.
6 D. W. de Quilettes, S. M. Vorpahl, S. D. Stranks, H. Nagaoka, G. E. Eperon, M. E. Ziffer, H. J. Snaith and D. S. Ginger, *Science*, 2015, **348**, 683–686.
7 Z. W. Xiao, Z. M. Song and Y. F. Yan, *Adv. Mater.*, 2019, **31**, 1803792.
8 Z. Shi, X. Sun, D. Wu, T. Xu, S. Zhuang, Y. Tian, X. Li and G. Du, *Nanoscale*, 2016, **8**, 10035–10042.
9 X. T. Zhang, H. Wang, Y. Hu, Y. X. Pei, S. X. Wang, Z. F. Shi, V. L. Colvin, S. N. Wang, Y. Zhang and W. W. Yu, *J. Phys. Chem. Lett.*, 2019, **10**, 1750–1756.

10 Z. Shi, Y. Li, Y. Zhang, Y. Chen, X. Li, D. Wu, T. Xu, C. Shan and G. Du, *Nano Lett.*, 2017, **17**, 313–321.
11 R. Dong, Y. J. Fang, J. Chae, J. Dai, Z. G. Xiao, Q. F. Dong, Y. B. Yuan, A. Centrone, X. C. Zeng and J. S. Huang, *Adv. Mater.*, 2015, **27**, 1912–1918.
12 D. H. Kwak, D. H. Lim, H. S. Ra, P. Ramasamy and J. S. Lee, *RSC Adv.*, 2016, **6**, 65252–65256.
13 H. Wang and D. H. Kim, *Chem. Soc. Rev.*, 2017, **46**, 5204–5236.
14 M. Ahmadi, T. Wu and B. Hu, *Adv. Mater.*, 2017, **29**, 1605242.
15 W. Tian, H. P. Zhou and L. Li, *Small*, 2017, **13**, 1702107.
16 Y. Li, Z. Shi, L. Lei, Z. Ma, F. Zhang, S. Li, D. Wu, T. Xu, X. Li, C. Shan and G. Du, *ACS Photonics*, 2018, **5**, 2524–2532.
17 M. J. Li, Q. Wei, S. K. Muduli, N. Yantara, Q. Xu, N. Mathews, S. G. Mhaisalkar, G. C. Xing and T. C. Sum, *Adv. Mater.*, 2018, **30**, 1707235.
18 H. Zhou, S. P. Yuan, X. X. Wang, T. Xu, X. Wang, H. L. Li, W. H. Zheng, P. Fan, Y. Y. Li, L. T. Sun and A. L. Pan, *ACS Nano*, 2017, **11**, 1189–1195.
19 Q. Zhang, R. Su, X. F. Liu, J. Xing, T. C. Sum and Q. H. Xiong, *Adv. Funct. Mater.*, 2016, **26**, 6238–6245.
20 Y. G. Wang, M. Yasar, Z. Y. Luo, S. S. Zhou, Y. W. Yu, H. Q. Li, R. Yang, X. X. Wang, A. L. Pan, L. Gan and T. Y. Zhai, *Small*, 2018, **14**, 1803010.
21 Z. Shi, X. Sun, D. Wu, T. Xu, Y. Tian, Y. Zhang, X. Li and G. Du, *J. Mater. Chem. C*, 2016, **4**, 8373–8379.
22 W. Lee, J. Lee, H. W. Yun, J. Kim, J. Park, C. Choi, D. Kim, H. Seo, H. Lee, J. Yu, W. Lee and D. Kim, *Adv. Mater.*, 2017, **29**, 1702902.
23 K. L. Xia, W. Q. Wu, M. J. Zhu, X. Y. Shen, Z. Yin, H. M. Wang, S. Li, M. C. Zhang, H. M. Wang, H. J. Lu, A. L. Pan, C. F. Pan and Y. Y. Zhang, *Sci. Bull.*, 2020, **65**, 343–349.
24 C. L. Li, H. L. Wang, F. Wang, T. F. Li, M. J. Xu, H. Wang, Z. Wang, X. W. Zhan, W. D. Hu and L. Shen, *Light: Sci. Appl.*, 2020, **9**, 31.
25 F. Rahimi, A. K. Jafari, C. A. Hsu, C. S. Ferekides and A. M. Hoff, *Org. Electron.*, 2019, **75**, 105397.
26 W. Liang, Z. Shi, Y. Li, J. Ma, S. Yin, X. Chen, D. Wu, Y. Tian, Y. Tian, Y. Zhang, X. Li and C. Shan, *ACS Appl. Mater. Interfaces*, 2020, **12**, 37363–37374.
27 M. Vasilopoulou, B. S. Kim, H. P. Kim, W. Silva, F. K. Schneider, M. A. M. Teridi, P. Gao, A. Yusoff and M. Nazeeruddin, *Nano Lett.*, 2020, **20**, 5081–5089.
28 B. X. Li, H. Yin, F. Xia, B. Sun, S. Y. Zhang, Y. D. Xia, Y. H. Chen and W. Huang, *Adv. Electron. Mater.*, 2020, **6**, 2000109.
29 G. Cao, C. T. Cheng, H. J. Zhang, H. Zhang, R. Chen, B. J. Huang, X. B. Yan, W. H. Pei and H. D. Chen, *J. Semicond.*, 2020, **41**, 051205.
30 S. Lee, H. Kim, D. Kim, W. Kim, J. Lee, J. Choi, H. Shin, G. Han, H. W. Jang and H. Jung, *ACS Appl. Mater. Interfaces*, 2020, **12**, 17039–17045.
31 Y. Li, Z. Shi, X. Li and C. Shan, *Chin. Phys. B*, 2019, **28**, 017803.
32 J. W. Lu, X. X. Sheng, G. Q. Tong, Z. W. Yu, X. L. Sun, L. W. Yu, X. X. Xu, J. Z. Wang, J. Xu, Y. Shi and K. J. Chen, *Adv. Mater.*, 2017, **29**, 1700400.
33 J. Chen, Y. P. Fu, L. Samad, L. Dang, Y. Z. Zhao, S. H. Shen, L. J. Guo and S. Jin, *Nano Lett.*, 2017, **17**, 460–466.
34 B. Yang, F. Y. Zhang, J. S. Chen, S. Q. Yang, X. S. Xia, T. Pullerits, W. Q. Deng and K. L. Han, *Adv. Mater.*, 2017, **29**, 1703758.
35 Y. Li, Z. Shi, S. Li, L. Lei, H. Ji, D. Wu, T. Xu, Y. Tian and X. Li, *J. Mater. Chem. C*, 2017, **5**, 8355–8360.
36 M. G. Ju, M. Chen, Y. Y. Zhou, J. Dai, L. Ma, N. P. Padture and X. C. Zeng, *Joule*, 2018, **2**, 1–11.
37 J. J. Luo, M. C. Hu, G. D. Niu and J. Tang, *ACS Appl. Mater. Interfaces*, 2019, **11**, 31575–31584.
38 Z. Ma, L. Wang, X. Ji, X. Chen and Z. Shi, *J. Phys. Chem. Lett.*, 2020, **11**, 5517–5530.
39 N. C. Miller and M. Bernechea, *APL Mater.*, 2018, **6**, 084503.
40 S. Attique, N. Ali, S. Ali, R. Khatoon, N. Li, A. Khesro, S. Rauf, S. Yang and H. Wu, *Adv. Sci.*, 2020, **7**, 1903143.
41 I. Park, L. Chu, K. Leng, Y. Choy, W. Liu, I. Abdelwahab, Z. Zhu, Z. Ma, W. Chen, Q. Xu, G. Eda and K. Loh, *Adv. Funct. Mater.*, 2019, **29**, 1904810.
42 J. Zhou, J. J. Luo, X. M. Rong, P. J. Wei, M. Molokeev, Y. Huang, J. Zhao, Q. Liu, X. W. Zhang, J. Tang and Z. G. Xia, *Adv. Opt. Mater.*, 2019, **7**, 1900139.
43 A. A. Hussain, A. K. Rana and M. Ranjan, *Nanoscale*, 2019, **11**, 1217–1227.
44 B. Pradhan, S. K. Kumar, S. Sain, A. Dalui, U. K. Ghorai, S. K. Pradhan and S. Acharya, *Chem. Mater.*, 2018, **30**, 2135–2142.
45 J. J. Luo, S. R. Li, H. D. Wu, Y. Zhou, Y. Li, J. Liu, J. H. Li, K. H. Li, F. Yi, G. D. Niu and J. Tang, *ACS Photonics*, 2018, **5**, 398–405.
46 P. M. Jayasankar, A. Pathak, S. Madhusudanan, S. Murali and S. Batabyal, *Mater. Lett.*, 2020, **263**, 127200.
47 H. W. Zhou, X. J. Liu, G. H. He, L. Fan, S. Z. Shi, J. Z. Wei, W. L. Xu, C. Yuan, N. Chai, B. L. Chen, Y. T. Zhang, X. X. Zhang, J. S. Zhao, X. T. Wei, J. Yin and D. X. Tian, *ACS Omega*, 2018, **3**, 14021–14026.
48 T. Zhu, Y. R. Yang and X. Gong, *ACS Appl. Mater. Interfaces*, 2020, **12**, 26776–26811.
49 L. S. Liang and P. Gao, *Adv. Sci.*, 2018, **5**, 1700331.
50 C. C. Wu, Q. H. Zhang, G. H. Liu, Z. H. Zhang, D. Wang, B. Qu, Z. J. Chen and L. X. Xiao, *Adv. Energy Mater.*, 2019, **10**, 1902496.
51 P. Umari, E. Mosconi and F. D. Angelis, *Sci. Rep.*, 2015, **4**, 4467.
52 B. W. Park, B. Philippe, X. Zhang, H. Rensmo, G. Boschloo and E. M. Johansson, *Adv. Mater.*, 2015, **27**, 6806–6813.
53 I. Benabdallah, M. Boujnah, A. El Kenz, A. Benyoussef, M. Abatal and A. Bassam, *J. Alloys Compd.*, 2019, **773**, 796–801.
54 B. W. Park, B. Philippe, X. L. Zhang, H. Rensmo, G. Boschloo and M. J. Johansson, *Adv. Mater.*, 2015, **27**, 6806–6813.
55 T. Singh, A. Kulkarni, M. Ikegami and T. Miyasaka, *ACS Appl. Mater. Interfaces*, 2016, **8**, 14542–14547.

56 K. Eckhardt, V. Bon, J. Getzschmann, J. Grothe, F. M. Wisser and S. Kaskel, *Chem. Commun.*, 2016, **52**, 3058–3060.
57 J. C. Hebig, I. Kühn, J. Flohre and T. Kirchartz, *ACS Energy Lett.*, 2016, **1**, 309–314.
58 C. T. Zuo and L. M. Ding, *Angew. Chem., Int. Ed.*, 2017, **56**, 6528–6532.
59 F. Y. Jiang, D. W. Yang, Y. Y. Jiang, T. F. Liu, X. G. Zhao, Y. Ming, B. W. Luo, F. Qin, J. C. Fan, H. W. Han, L. J. Zhang and Y. H. Zhou, *J. Am. Chem. Soc.*, 2018, **140**, 1019–1027.
60 P. V. Harikesh, H. K. Mulmudi, B. Ghosh, T. W. Goh, Y. T. Teng, K. Thirumal, M. Lockrey, K. Weber, T. M. Koh, S. Z. Li, S. Mhaisalkar and N. Mathews, *Chem. Mater.*, 2016, **28**, 7496–7504.
61 Y. X. Zhang, Y. C. Liu, Z. Xu, H. C. Ye, Z. Yang, J. X. You, M. Liu, Y. H. He, M. G. Kanatzidis and S. Z. Liu, *Nat. Commun.*, 2020, **11**, 2304.
62 Z. Z. Ma, Z. F. Shi, L. T. Wang, F. Zhang, D. Wu, D. W. Yang, X. Chen, Y. Zhang, C. X. Shan and X. J. Li, *Nanoscale*, 2020, **12**, 3637–3645.
63 Z. Z. Ma, Z. F. Shi, D. W. Yang, F. Zhang, S. Li, L. T. Wang, D. Wu, Y. T. Zhang, G. R. Na, L. J. Zhang, X. J. Li, Y. Zhang and C. X. Shan, *ACS Energy Lett.*, 2020, **5**, 385–394.
64 X. G. Zhao, J. H. Yang, Y. H. Fu, D. W. Yang, Q. L. Xu, L. P. Yu, S. H. Wei and L. J. Zhang, *J. Am. Chem. Soc.*, 2017, **139**, 2630–2638.
65 Y. Li, Z. F. Shi, L. Z. Lei, S. Li, D. W. Yang, D. Wu, T. T. Xu, Y. Z. Tian, Y. J. Lu, Y. Wang, L. J. Zhang, X. J. Li, Y. T. Zhang, G. T. Du and C. X. Shan, *Adv. Mater. Interfaces*, 2019, **6**, 1900188.
66 J. Xu, J. B. Liu, B. X. Liu and B. Huang, *J. Phys. Chem. Lett.*, 2017, **8**, 4391–4396.
67 E. T. McClure, M. R. Ball, W. Windl and P. M. Woodward, *Chem. Mater.*, 2016, **28**, 1348–1354.
68 M. R. Filip, X. L. Liu, A. Miglio, G. Hautier and F. Giustino, *J. Phys. Chem. C*, 2018, **122**, 158–170.
69 P. F. Cheng, L. Sun, L. Feng, S. Q. Yang, Y. Yang, D. Y. Zheng, Y. Zhao, Y. B. Sang, R. L. Zhang, D. H. Wei, W. Q. Deng and K. L. Han, *Angew. Chem., Int. Ed.*, 2019, **58**, 16087–16091.
70 J. W. Li, Q. Yu, Y. H. He, C. C. Stoumpos, G. D. Niu, G. G. Trimarchi, H. Guo, G. F. Dong, D. Wang, L. D. Wang and M. G. Kanatzidis, *J. Am. Chem. Soc.*, 2018, **140**, 11085–11090.
71 L. Zhou, J. F. Liao, Z. G. Huang, J. H. Wei, X. D. Wang, H. Y. Chen and D. B. Kuang, *Angew. Chem., Int. Ed.*, 2019, **58**, 15435–15440.
72 L. T. Wang, Z. F. Shi, Z. Z. Ma, D. W. Yang, F. Zhang, X. Z. Ji, M. Wang, X. Chen, G. R. Na, S. Chen, D. Wu, Y. Zhang, X. J. Li, L. J. Zhang and C. X. Shan, *Nano Lett.*, 2020, **20**, 3568–3576.
73 A. Waleed, M. Tavakoli, L. Gu, Z. Y. Wang, D. Zhang, A. Manikandan, Q. P. Zhang, R. J. Zhang, Y. Chueh and Z. Y. Fan, *Nano Lett.*, 2017, **17**, 523–530.
74 Z. T. Du, D. F. Fu, T. Yang, Z. Fang, W. N. Liu, F. M. Gao, L. Wang, Z. B. Yang, J. Teng, H. Zhang and W. Y. Yang, *J. Mater. Chem. C*, 2018, **6**, 6287–6296.
75 J. Im, C. C. Stoumpos, H. Jin, A. J. Freeman and M. G. Kanatzidis, *J. Phys. Chem. Lett.*, 2015, **6**, 3503–3509.
76 H. L. Zhu, H. Liu, Z. L. Song, Z. Wang, F. Ye, H. Zhang, W. J. Yin, Y. F. Yan and W. Choy, *ACS Nano*, 2019, **13**, 11800–11808.
77 Y. Wang, C. D. Chen, T. Y. Zou, L. Z. Yan, C. Liu, X. Z. Du, S. D. Zhang and H. Zhou, *Adv. Mater. Technol.*, 2019, **5**, 1900752.
78 Y. Wang, D. Z. Yang, D. Ma, D. Kim, T. Ahamad, S. Alshehri and A. Vadim, *Sci. China Mater.*, 2019, **62**, 790–796.
79 L. Qian, Y. Sun, M. Wu, C. Li, D. Xie, L. M. Ding and G. Q. Shi, *Nanoscale*, 2018, **10**, 6837–6843.
80 C. Liu, Q. Tai, N. X. Wang, G. Q. Tang, H. Loi and F. Yan, *Adv. Sci.*, 2019, **6**, 1900751.
81 X. Han, J. Liang, J. H. Yang, K. Soni, Q. Y. Fang, W. P. Wang, J. Zhang, S. Jia, A. A. Martí, Y. Zhao and J. Lou, *Small*, 2019, **15**, 1901650.
82 D. L. Shao, W. G. Zhu, G. Q. Xin, J. Lian and S. Sawyer, *Appl. Phys. Lett.*, 2019, **115**, 121106.
83 K. M. McCall, C. C. Stoumpos, S. S. Kostina, M. G. Kanatzidis and B. W. Wessels, *Chem. Mater.*, 2017, **29**, 4129–4145.
84 X. W. Tong, W. Y. Kong, Y. Y. Wang, J. M. Zhu, L. B. Luo and Z. H. Wang, *ACS Appl. Mater. Interfaces*, 2017, **9**, 18977–18985.
85 S. Premkumar, D. Liu, Y. M. Zhang, D. Nataraj, S. Ramya, Z. Z. Jin, B. B. Mamba, A. T. Kuvarega and J. Z. Gui, *ACS Appl. Nano Mater.*, 2020, **3**, 9141–9150.
86 A. A. Hussain, *ACS Appl. Mater. Interfaces*, 2020, **12**, 46317–46329.
87 J. K. Pious, A. Katre, C. Muthu, S. Chakraborty, S. Krishna and V. C. Nair, *Chem. Mater.*, 2019, **31**, 1941–1945.
88 Z. Y. Qi, X. W. Fu, T. F. Yang, D. Li, P. Fan, H. L. Li, F. Jiang, L. H. Li, Z. Y. Luo, X. J. Zhuang and A. L. Pan, *Nano Res.*, 2019, **12**, 1894–1899.
89 W. G. Li, X. D. Wang, J. F. Liao, Y. Jiang and D. B. Kuang, *Adv. Funct. Mater.*, 2020, **30**, 1909701.
90 H. J. Zhang, Y. D. Xu, Q. H. Sun, J. P. Dong, Y. F. Lu, B. B. Zhang and W. Q. Jie, *CrystEngComm*, 2018, **20**, 4935–4941.
91 Q. H. Sun, Y. D. Xu, H. J. Zhang, B. Xiao, X. Liu, J. P. Dong, Y. B. Cheng, B. B. Zhang, W. Q. Jie and M. G. Kanatzidis, *J. Mater. Chem. A*, 2018, **6**, 23388–23395.
92 W. C. Zhang, Y. Sui, B. Kou, Y. Peng, Z. Y. Wu and J. H. Luo, *ACS Appl. Mater. Interfaces*, 2020, **12**, 9141–9149.
93 C. M. Ji, P. Wang, Z. Y. Wu, Z. H. Sun, L. Li, J. Zhang, W. D. Hu, M. C. Hong and J. H. Luo, *Adv. Funct. Mater.*, 2018, **28**, 1705467.
94 M. L. Xia, J. H. Yuan, G. D. Niu, X. Y. Du, L. X. Yin, W. C. Pan, J. J. Luo, Z. G. Li, H. T. Zhao, K. H. Xue, X. S. Miao and J. Tang, *Adv. Funct. Mater.*, 2020, **30**, 1910648.
95 Y. C. Liu, Z. Xu, Z. Yang, Y. X. Zhang, J. Cui, Y. H. He, H. C. Ye, K. Zhao, H. M. Sun, R. Lu, M. Liu, M. G. Kanatzidis and S. Z. Liu, *Matter*, 2020, **3**, 1–17.
96 B. Saparov, F. Hong, J. P. Sun, H. S. Duan, W. Meng, S. Cameron, I. G. Hill, Y. Yan and D. B. Mitzi, *Chem. Mater.*, 2015, **27**, 5622–5632.

97 J. Pal, S. Manna, A. Mondal, S. Das, K. V. Adarsh and A. Nag, *Angew. Chem., Int. Ed.*, 2017, **56**, 14187–14191.
98 A. Singh, K. M. Boopathi, A. Mohapatra, Y. F. Chen, G. Li and C. W. Chu, *ACS Appl. Mater. Interfaces*, 2018, **10**, 2566–2573.
99 Z. Zheng, Q. S. Hu, H. Z. Zhou, P. Luo, A. Nie, H. M. Zhu, L. Gan, F. W. Zhuge, Y. Ma, H. S. Song and T. Y. Zhai, *Nanoscale Horiz.*, 2019, **4**, 1372–1379.
100 B. Yang, Y. J. Li, Y. X. Tang, X. Mao, C. Luo, M. S. Wang, W. Q. Deng and K. L. Han, *J. Phys. Chem. Lett.*, 2018, **9**, 3087–3092.
101 Y. L. Lei, S. Y. Wang, J. Xing, H. Xu, J. Han and W. F. Liu, *Inorg. Chem.*, 2020, **59**, 4349–4356.
102 W. C. Pan, H. D. Wu, J. J. Luo, Z. Z. Deng, C. Ge, C. Chen, X. W. Jiang, W. J. Yin, G. D. Niu, L. J. Zhu, L. X. Yin, Y. Zhou, Q. G. Xie, X. X. Ke, M. L. Sui and J. Tang, *Nat. Photonics*, 2017, **11**, 726–732.
103 L. Z. Lei, Z. F. Shi, Y. Li, Z. Z. Ma, F. Zhang, T. T. Xu, Y. T. Tian, D. Wu, X. J. Li and G. T. Du, *J. Mater. Chem. C*, 2018, **6**, 7982–7988.
104 C. C. Wu, B. W. Du, W. Luo, Y. Liu, T. Y. Li, D. Wang, X. Guo, H. Ting, Z. Y. Fang, S. F. Wang, Z. J. Chen, Y. X. Chen and L. X. Xiao, *Adv. Opt. Mater.*, 2018, **6**, 1800811.
105 W. N. Yuan, G. D. Niu, Y. M. Xian, H. D. Wu, H. M. Wang, H. Yin, P. Liu, W. Z. Li and J. D. Fan, *Adv. Funct. Mater.*, 2019, **29**, 1900234.
106 B. Yang, W. C. Pan, H. D. Wu, G. D. Niu, J. H. Yuan, K. H. Xue, L. X. Yin, X. Y. Du, X. S. Miao, X. Q. Yang, Q. G. Xie and J. Tang, *Nat. Commun.*, 2019, **10**, 1989.
107 J. Yang, C. X. Bao, W. H. Ning, B. Wu, F. X. Ji, Z. B. Yan, Y. T. Tao, J. M. Liu, T. C. Sum, S. Bai, J. P. Wang, W. Huang, W. J. Zhang and F. Gao, *Adv. Opt. Mater.*, 2019, **7**, 1801732.
108 Z. Y. Xu, X. Liu, Y. B. Li, X. T. Liu, T. Yang, C. M. Ji, S. G. Han, Y. D. Xu, J. H. Luo and Z. H. Sun, *Angew. Chem., Int. Ed.*, 2019, **58**, 15857–15861.
109 T. Li, J. Wang, Z. Y. Gao, P. Lv, Y. B. Yang, J. S. Wu, J. W. Hong, X. Y. Wang and Y. W. Zhou, *Appl. Phys. Lett.*, 2019, **115**, 131103.
110 L. X. Yin, H. D. Wu, W. C. Pan, B. Yang, P. H. Li, J. J. Luo, G. D. Niu and J. Tang, *Adv. Opt. Mater.*, 2019, **7**, 1900491.
111 G. H. Yan, B. Q. Jiang, Y. Yuan, M. Kuang, X. Y. Liu, Z. H. Zeng, C. X. Zhao, J. He and W. J. Mai, *ACS Appl. Mater. Interfaces*, 2020, **12**, 6064–6073.
112 M. Wang, P. Zeng, Z. H. Wang and M. Z. Liu, *Adv. Sci.*, 2020, **7**, 1903662.
113 Y. Y. Dang, G. Q. Tong, W. T. Song, Z. H. Liu, L. B. Qiu, L. Ono and Y. B. Qi, *J. Mater. Chem. C*, 2020, **8**, 276–284.
114 E. Greul, M. L. Petrus, A. Binek, P. Docampo and T. Bein, *J. Mater. Chem. A*, 2017, **5**, 19972–19981.
115 B. Vargas, E. Ramos, E. Pérez-Gutiérrez, J. C. Alonso and D. Solis-Ibarra, *J. Am. Chem. Soc.*, 2017, **139**, 9116–9119.
116 Z. Deng, F. Wei, S. Sun, G. Kieslich, A. K. Cheetham and P. D. Bristowe, *J. Mater. Chem. A*, 2016, **4**, 12025–12029.
117 W. Zhou, P. G. Han, X. R. Zhang, D. Y. Zheng, S. Q. Yang, Y. Yang, C. Luo, B. Yang, F. Hong, D. H. Wei, R. F. Lu and K. L. Han, *J. Phys. Chem. Lett.*, 2020, **11**, 6463–6467.
118 G. Volonakis, A. A. Haghighirad, R. L. Milot, W. H. Sio, M. R. Filip, B. Wenger, M. B. Johnston, L. M. Herz, H. J. Snaith and F. Giustino, *J. Phys. Chem. Lett.*, 2017, **8**, 772–778.
119 W. Meng, X. Wang, Z. Xiao, J. Wang, D. B. Mitzi and Y. Yan, *J. Phys. Chem. Lett.*, 2017, **8**, 2999–3007.
120 A. H. Slavney, L. Leppert, A. S. Valdes, D. Bartesaghi, T. J. Savenije, J. B. Neaton and H. I. Karunadasa, *Angew. Chem.*, 2018, **130**, 12947–12952.
121 Y. Li, Z. F. Shi, W. Q. Liang, L. T. Wang, S. Li, F. Zhang, Z. Z. Ma, Y. Wang, Y. Z. Tian, D. Wu, X. J. Li, Y. T. Zhang, C. X. Shan and X. S. Fang, *Mater. Horiz.*, 2020, **7**, 530–540.
122 F. J. Zeng, Y. Y. Guo, W. Hu, Y. Q. Tan, X. M. Zhang, J. Yang, Q. Q. Lin, Y. Peng, X. S. Tang, Z. Z. Liu, Z. Q. Yao and J. Du, *J. Semicond.*, 2020, **223**, 117178.
123 W. Q. Liang, Y. Li, J. L. Ma, Y. Wang, J. J. Yan, X. Chen, D. Wu, Y. T. Tian, X. J. Li and Z. F. Shi, *Nanoscale*, 2020, **12**, 17213–17221.
124 Z. Z. Ma, Z. F. Shi, C. C. Qin, M. H. Cui, D. W. Yang, X. J. Wang, L. T. Wang, X. Z. Ji, X. Chen, J. L. Sun, D. Wu, Y. Zhang, X. J. Li, L. J. Zhang and C. X. Shan, *ACS Nano*, 2020, **14**, 4475–4486.
125 J. Yang, W. Kang, Z. Z. Liu, M. Y. Pi, L. B. Luo, C. Li, H. Lin, Z. T. Luo, J. Du, M. Zhou and X. S. Tang, *J. Phys. Chem. Lett.*, 2020, **11**, 6880–6886.
126 Z. X. Zhang, C. Li, Y. Lu, X. W. Tong, F. X. Liang, X. Y. Zhao, D. Wu, C. Xie and L. B. Luo, *J. Phys. Chem. Lett.*, 2019, **10**, 5343–5350.
127 N. Liu, X. Zhao, M. L. Xia, G. D. Niu, Q. X. Guo, L. Gao and J. Tang, *J. Semicond.*, 2020, **41**, 052204.
128 T. Jun, K. Sim, S. Limura, M. Sasase, H. Kamioka, J. Kim and H. Hosono, *Adv. Mater.*, 2018, **30**, 1804547.
129 H. Peng, B. S. Zou, Y. C. Guo, R. N. Zhi, X. X. Wang, S. F. Yao, F. J. Ge, Y. Tian, J. P. Wang and B. S. Zou, *J. Phys. Chem. Lett.*, 2020, **11**, 4703–4710.
130 R. C. Lin, Q. L. Guo, Q. Zhu, Y. M. Zhu, W. Zheng and F. Huang, *Adv. Mater.*, 2019, **31**, 1905079.
131 Y. Li, Z. F. Shi, L. T. Wang, Y. C. Chen, W. Q. Liang, D. Wu, X. J. Li, Y. Zhang, C. X. Shan and X. S. Fang, *Mater. Horiz.*, 2020, **7**, 1613–1622.
132 Z. Q. Li, Z. L. Li, Z. F. Shi and X. S. Fang, *Adv. Funct. Mater.*, 2020, **30**, 2002634.
133 B. Yang, L. X. Yin, G. D. Niu, J. H. Yuan, K. H. Xue, Z. F. Tan, X. S. Miao, M. Niu, X. Y. Du, H. S. Song, E. Lifshitz and J. Tang, *Adv. Mater.*, 2019, **31**, 1904711.
134 L. Zhou, J. F. Liao, Z. G. Huang, J. H. Wei, X. D. Wang, W. G. Li, H. Y. Chen, D. B. Kuang and C. Y. Su, *Angew. Chem., Int. Ed.*, 2019, **58**, 5277–5281.
135 X. Y. Liu, X. Xu, B. Li, Y. Q. Liang, Q. Li, H. Jiang and D. S. Xu, *CCS Chem.*, 2020, **2**, 216–224.
136 X. M. Tang, H. Zhou, X. Y. Pan, R. H. Liu, D. J. Wu and H. Wang, *ACS Appl. Mater. Interfaces*, 2020, **12**, 4843–4848.
137 Y. Zhao, C. L. Li, J. Z. Jiang, B. M. Wang and L. Shen, *Small*, 2020, **16**, 2001534.
138 B. H. Li, R. Y. Long, Q. S. Yao, Z. H. Zhu and Q. X. Mi, *J. Phys. Chem. Lett.*, 2019, **10**, 3699–3703.

139 M. M. Han, J. M. Sun, M. Peng, N. Han, Z. H. Chen, D. Liu, Y. N. Guo, S. Zhao, C. X. Shan, T. Xu, X. T. Hao, W. D. Hu and Z. X. Yang, *J. Phys. Chem. C*, 2019, **123**, 17566–17573.
140 D. Liu, B. B. Yu, M. Liao, Z. X. Jin, L. Zhou, X. X. Zhang, F. Y. Wang, H. T. He, T. Gatti and Z. B. He, *ACS Appl. Mater. Interfaces*, 2020, **12**, 30530–30537.
141 Y. Y. Tang, M. L. Liang, B. D. Chang, H. Y. Sun, K. B. Zheng, T. Pullerits and Q. J. Chi, *J. Mater. Chem. C*, 2019, **7**, 3369–3374.
142 P. Liu, Y. Liu, S. W. Zhang, J. Z. Li, C. Y. Wang, C. Zhao, P. B. Nie, Y. H. Dong, X. Zhang, S. X. Zhao and G. D. Wei, *Adv. Opt. Mater.*, 2020, **8**, 2001072.
143 C. S. Yang, D. S. Shang, N. Liu, G. Shi, X. Shen, R. C. Yu, Y. Q. Li and Y. Sun, *Adv. Mater.*, 2017, **29**, 1700906.
144 P. Gkoupidenis, N. Schaefer, B. Garlan and G. G. Malliaras, *Adv. Mater.*, 2015, **27**, 7176–7180.
145 D. B. Strukov, G. S. Snider, D. R. Stewart and R. S. Williams, *Nature*, 2008, **453**, 80–83.
146 A. A. Bessonov, M. N. Kirikova, D. I. Petukhov, M. Allen, T. Ryhänen and M. J. Bailey, *Nat. Mater.*, 2015, **14**, 199–204.
147 L. D. Li, Z. Lou and G. Z. Shen, *Adv. Funct. Mater.*, 2017, **28**, 1705389.
148 W. Deng, X. J. Zhang, L. M. Huang, X. Z. Xu, L. Wang, J. C. Wang, Q. X. Shang, S. T. Lee and J. S. Jie, *Adv. Mater.*, 2016, **28**, 2201–2208.
149 S. Yakunin, M. Sytnyk, D. Kriegner, S. Shrestha, M. Richter, G. J. Matt, H. Azimi, C. J. Brabec, J. Stangl, M. V. Kovalenko and W. Heiss, *Nat. Photonics*, 2015, **9**, 444–449.
150 H. T. Wei, Y. J. Fang, P. Mulligan, W. Chuirazzi, H.-H. Fang, C. C. Wang, B. R. Ecker, Y. L. Gao, M. A. Loi, L. Cao and J. S. Huang, *Nat. Photonics*, 2016, **10**, 333–339.
151 S. Yakunin, D. N. Dirin, Y. Shynkarenko, V. Morad, I. Cherniukh, O. Nazarenko, D. Kreil, T. Nauser and M. V. Kovalenko, *Nat. Photonics*, 2016, **10**, 585–589.
152 Y. C. Liu, Y. X. Zhang, Z. Yang, J. Cui, H. D. Wu, X. D. Ren, K. Zhao, J. S. Feng, J. Tang, Z. Xu and S. Z. Liu, *Adv. Opt. Mater.*, 2020, **8**, 2000814.
153 S. J. Tie, W. Zhao, D. Y. Xin, M. Zhang, J. D. Long, Q. Chen, X. J. Zheng, J. G. Zhu and W. H. Zhang, *Adv. Mater.*, 2020, **32**, 2001981.